



Cite this: DOI: 10.1039/d2qi00601d

Single-ion magnet behaviour in homoleptic Co(II) complexes bearing 2-iminopyrrolyl ligands†

Patrícia S. Ferreira,^a Ana C. Cerdeira,^b Tiago F. C. Cruz,^a Nuno A. G. Bandeira,^c David Hunger,^d Alexander Allgaier,^d Joris van Slageren,^d Manuel Almeida,^b Laura C. J. Pereira^b and Pedro T. Gomes^a

In this report we present the structural and magnetic characterization of four distorted tetrahedral homoleptic Co(II) complexes bearing two 2-formiminopyrrolyl *N,N'*-chelating ligands, [Co(κ^2N,N' -NC₄H₃-2-C(H)=N(2,6-¹Pr₂-C₆H₃))₂] (**1**), [Co(κ^2N,N' -5-(C₆H₅)-NC₄H₂-2-C(H)=N(2,6-¹Pr₂-C₆H₃))₂] (**2**), [Co(κ^2N,N' -5-(2,6-Me₂-C₆H₃)-NC₄H₂-2-C(H)=N(2,6-¹Pr₂-C₆H₃))₂] (**3**) and [Co(κ^2N,N' -5-(1-Ad)-NC₄H₂-2-C(H)=N(1-Ad))₂] (Ad = adamantyl) (**4**), which display Single-Ion Magnet (SIM) behaviour. Static (dc) magnetic susceptibility measurements and high-field EPR spectroscopy showed a large and negative magnetic anisotropy with values of $D = -69, -53, -48$ and -52 cm⁻¹ for complexes **1–4**, respectively. These values are interpreted and reproduced by means of theoretical calculations (*ab initio* CASSCF/QD-NEVPT2 methods) where it was shown that the most important source of axial anisotropy stems from the first $e \rightarrow t_2$ electronic transition, in line with other tetrahedrally coordinated Co(II) complexes. Calculations on model systems show that the most favorable magnetostructural modification corresponds to a tetrahedral geometry with a strong distortion towards a trigonal based pyramid. Frequency-dependent (ac) magnetic susceptibility measurements show that the 5-substituted pyrrolyl ring derivatives **2–4** display slow relaxation of the magnetization at zero external magnetic field, whereas the 5-unsubstituted-2-iminopyrrolyl complex **1** requires the presence of a static magnetic field to exhibit this property. By applying a static magnetic field, the quantum tunnelling of magnetization (QTM) process is suppressed revealing large energy barriers (U_{eff}) for all the complexes studied, exhibiting values of 138, 106, 96 and 104 cm⁻¹ for **1–4**, respectively. These values are higher than the majority of tetracoordinated Co(II)-based SIMs reported in the literature. Despite large values of axial zero-field splitting, as determined by theory, the experimental energy barriers are considerably lower than expected for a pure Orbach process, indicating that other relaxation mechanisms are dominant in the range of temperatures studied.

Received 21st March 2022

Accepted 31st May 2022

DOI: 10.1039/d2qi00601d

rsc.li/frontiers-inorganic

^aCentro de Química Estrutural, Institute of Molecular Sciences, Departamento de Engenharia Química, Instituto Superior Técnico, Universidade de Lisboa, Av. Rovisco Pais 1, 1049-001 Lisboa, Portugal. E-mail: pedro.t.gomes@tecnico.ulisboa.pt

^bCentro de Ciências e Tecnologias Nucleares, Departamento de Engenharia e Ciências Nucleares, Instituto Superior Técnico, Universidade de Lisboa, 2695-066 Bobadela LRS, Portugal. E-mail: lpereira@ctn.tecnico.ulisboa.pt

^cBioISI – Biosystems & Integrative Sciences Institute, Departamento de Química e Bioquímica, Faculdade de Ciências, Universidade de Lisboa, Campo Grande, Ed. C8, 1749-016 Lisboa, Portugal. E-mail: nabandeira@fc.ul.pt

^dInstitut für Physikalische Chemie, Universität Stuttgart, Pfaffenwaldring 55, Stuttgart D-70569, Germany. E-mail: slageren@ipc.uni-stuttgart.de

† Electronic supplementary information (ESI) available. CCDC 2160416. For ESI and crystallographic data in CIF or other electronic format see DOI: <https://doi.org/10.1039/d2qi00601d>

Introduction

Since the discovery of the first molecular material displaying slow relaxation of magnetization,¹ Single-Molecule Magnets (SMMs) have gained prominence due to their remarkable potential applications in data storage and processing, quantum computing and in molecular spintronics.² In these materials, due to the presence of an energy barrier for magnetization reversal, U_{eff} , the magnetization can be retained after the field has been removed. This barrier can be estimated under condition of axial symmetry (x, y equivalent) by $U_{\text{eff}} = S^2|D|$ for integer spin systems and $U_{\text{eff}} = (S^2 - \frac{1}{4})|D|$ for half-integer spin systems, where S is the total spin and D the axial component of the magnetic anisotropy.^{3,4} From these equations it would be expected that by increasing S , U_{eff} would also increase, although magnetic studies on polynuclear metal

complexes show that it does not increase proportionally.^{5,6} Therefore, the current focus lies on the design of new SMMs with a single magnetic centre (called Single-Ion Magnets, SIMs) enabling the enhancement of a negative magnetic anisotropy.

More than a decade after the discovery of the first compound with SMM behaviour, a dodecanuclear manganese cluster $[\text{Mn}_{12}\text{O}_{12}(\text{OOCMe})_{16}(\text{H}_2\text{O})_4]$, Single-Ion systems containing cheap and abundant d-block metal centres started to be the subject of intensive study. Since then, several tetra-coordinate $\text{Co}(\text{II})$ complexes showing SIM behaviour have been reported, but only a few showed slow relaxation of magnetization in the absence of an external magnetic field, with the corresponding values of D and U_{eff} varying within the ranges -70 to -161 cm^{-1} and 19 to 118 cm^{-1} , respectively.⁷⁻¹⁰ To the best of our knowledge, only five tetra-coordinate SIM-based $\text{Co}(\text{II})$ complexes containing four coordinating nitrogen atoms are found in the literature showing a strong magnetic anisotropy as a result of a strong axial distortion caused by the ligands (Chart 1).¹⁰⁻¹³ These are neutral, dianionic or dicationic distorted tetrahedral homoleptic complexes of $\text{Co}(\text{II})$ containing two symmetrical N,N -chelating ligands, which are, respectively, monoanionic triimidosulfonate (**A**), dianionic bisimido (**B**, **D** and **E**) and neutral bipyridine (**C**) moieties (Chart 1). All these complexes show high values of D but, with the exception of complex **B**,¹⁰ compounds **A**¹¹ and **C-E**^{12,13} have energy barriers lower than expected due to the predominance of the Raman relaxation process.

We have been interested in the coordination chemistry of asymmetrical bidentate N,N' -2-iminopyrrolyl and 5-substituted-

2-iminopyrrolyl monoanionic chelates, which are ligands somehow reminiscent of porphyrins. In recent years, we have prepared a good number of mono(2-iminopyrrolyl) complexes of first-row transition metals (Mn , Fe , Co , Ni , Cu),¹⁴ as well as of main-group elements (Na and B),¹⁵ the first group being employed as catalysts for various important organic reactions, and the second one, in the case of boron, as luminescent materials for OLED optoelectronic devices. We have also synthesized and characterized homoleptic bis(2-iminopyrrolyl) complexes of Fe , Co , Ni , Cu and Zn .¹⁶⁻¹⁸ Among the latter group, we have reported three highly electronically unsaturated homoleptic $\text{Co}(\text{II})$ complexes **1-3** (Chart 2),^{17,18} which showed large magnetic anisotropy through static magnetic measurements.

In order to understand whether SMM features could be on the basis of this anisotropy and how the ligand field and geometry of the complexes, namely the geometric distortion caused by the ligands, affect their SMM behaviour, four $\text{Co}(\text{II})$ complexes **1-4** of increasing steric bulk were studied in this work (Chart 2). Herein, we present the structural, magnetic, HFEP (High Field Electronic Paramagnetic Resonance spectroscopy) and theoretical studies of this family of distorted tetrahedral $\text{Co}(\text{II})$ complexes in an attempt to rationalize the SIM behaviour exhibited by all the four compounds studied.

Results and discussion

Syntheses and characterization of the ligands and complexes

Complexes **1**, **2** and **3** were synthesized according to the literature.^{17,18} The ligand precursor **II** and complex **4** were pre-

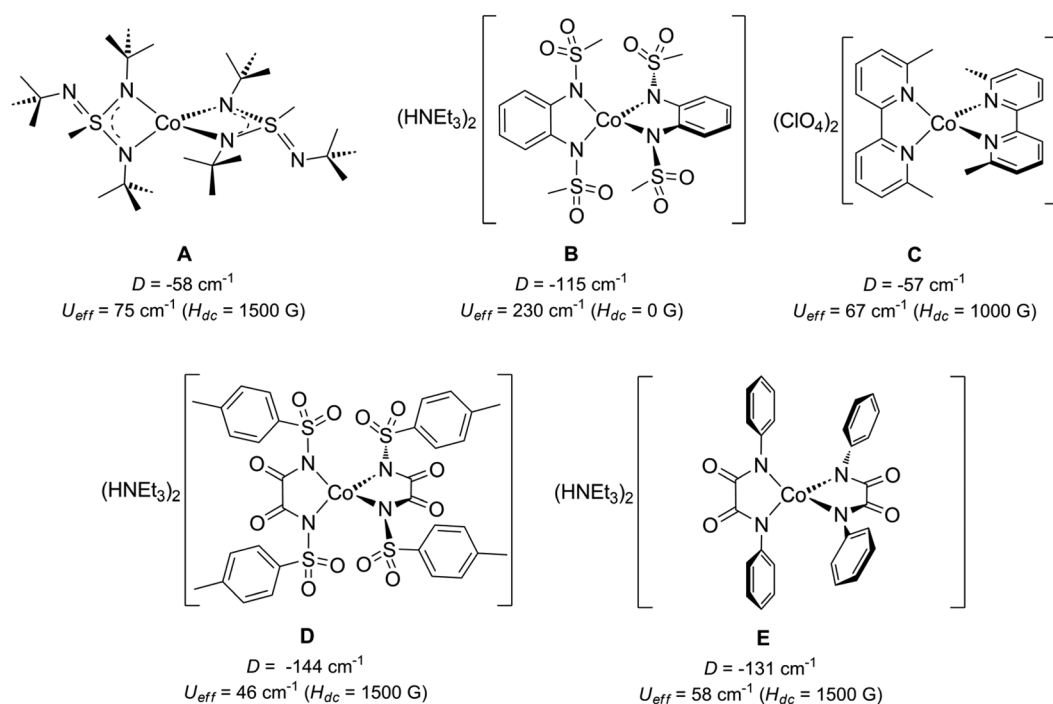


Chart 1 Tetrahedral N_4 -coordinated $\text{Co}(\text{II})$ complexes reported in the literature displaying SIM behaviour.

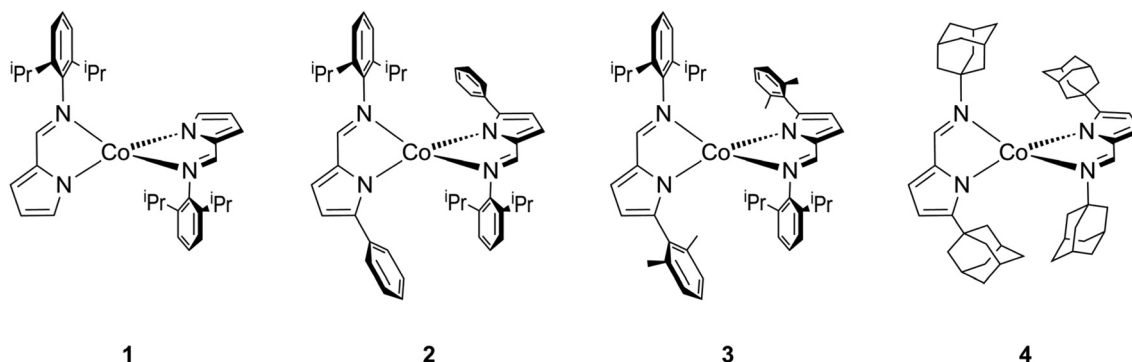
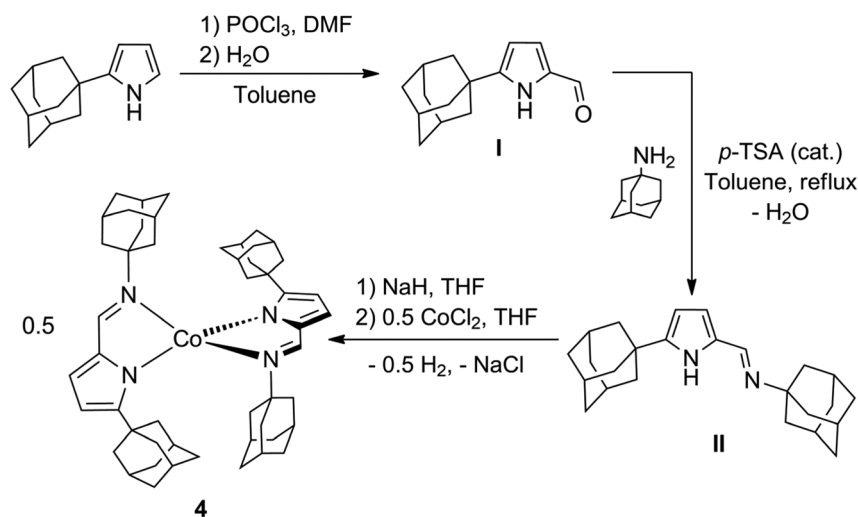


Chart 2 Complexes studied in this work.

pared under the same conditions as the corresponding previous ones (Scheme 1). The preparation of 2-(1-adamantyl)-1*H*-pyrrole was already reported in the literature, involving several reaction steps.¹⁹ 5-(1-Adamantyl)-2-formylpyrrole (**I**) was prepared from 2-(1-adamantyl)-1*H*-pyrrole through a classical Vilsmeier–Haack formylation reaction.²⁰ The new compound 5-(1-adamantyl)-2-(*N*-(1-adamantyl)formimino)pyrrole (**II**) was synthesized from a catalytic condensation reaction of **I** with 1-adamantylamine, in refluxing toluene. The homoleptic bis(2-iminopyrrolyl) complex **4** was obtained by the reaction of the *in situ* prepared sodium salt of the ligand precursor **II** with CoCl_2 in THF, with a molar ratio of 2 : 1, followed by crystallization in *n*-hexane at -20°C (Scheme 1).

Complex **4**, which is stable in air when in a crystalline state, was characterized by single crystal and powder X-ray diffraction, elemental analysis, FTIR and solution ^1H NMR spectroscopies, and magnetic susceptibility measurements in solution and in solid state. The FTIR spectrum of **4** shows a strong band at 1566 cm^{-1} , which is in the range of the

characteristic values of the $\text{C}=\text{N}$ bond stretching vibration (Fig. S1, in ESI[†]). Due to the paramagnetic nature of this complex, its ^1H NMR spectrum lies in the range $\delta -55$ to $+117$ (Fig. S2[†]). The effective magnetic moment, μ_{eff} , for compound **4** was measured in toluene- d_8 solution by the Evans method²¹ ($4.7\mu_{\text{B}}$) and in solid state by means of SQUID magnetometry ($5.13\mu_{\text{B}}$), both at room temperature. The experimental values of μ_{eff} measured for **4** lie within the range of known tetrahedral Co(II) complexes with $S = 3/2$, being similar to the other two 5-substituted-2-iminopyrrolyl complexes **2** and **3**¹⁸ (see Table S1 in ESI[†]), and are higher than the expected spin-only value of $3.88\mu_{\text{B}}$, which suggests the presence of spin–orbit coupling effects.^{17,18,22} A comparison of the experimental powder X-ray diffraction pattern of compound **4** with that of the theoretically predicted using the corresponding single crystal diffraction data proved that this structure represents the bulk of material studied. The same conclusion can be obtained for the samples of complexes 1–3 (see Fig. S3–S6 in ESI[†]).



Scheme 1 Synthesis of the new 5-(1-adamantyl)-2-(*N*-(1-adamantyl)formimino)pyrrole ligand precursor **II** and its corresponding homoleptic bis(2-iminopyrrolyl) Co(II) complex **4**.

Structural studies

Red prism single crystals of complex **4** suitable for X-ray diffraction were grown from a concentrated *n*-hexane solution cooled to $-20\text{ }^{\circ}\text{C}$. Complex **4** crystallizes in the monoclinic $P2_1/c$ space group, where two 5-(1-adamantyl)-2-iminopyrrolyl ligands are coordinated to the metal centre in a bidentate mode through the iminic (N2 and N4) and pyrrolyl (N1 and N3) nitrogen atoms in a distorted tetrahedral geometry, with a measure of the distortion given by the parameter τ_4 ²³ (0 for purely square planar and 1 for purely tetrahedral geometries). The molecular structure of complex **4** is shown in Fig. 1, and selected bond distances and angles are listed in Table S3 in ESI.† Important experimental structural parameters measured in the molecular structure of complex **4**, such as the chelating ligand bite angles (θ_1 and θ_2), the dihedral angle between planes of the chelating ligands (ϕ), the interligand angle (ω) and parameter τ_4 , which will be compared with the values used in a magnetostructural model study presented below in the Theoretical calculations section, are also listed in the same table. These values of complex **4** are also compiled in Table 1

(and also in Table S2†) together with the corresponding parameters of complexes **1–3**, which were calculated from the literature data,^{17,18} for the sake of a clearer comparison.

The intrinsic geometrical nature of the *N,N'*-2-iminopyrrolyl five-membered chelating ligand inflicts a significant deviation of the N–Co–N chelating bite angles θ (Tables 1 and S2†) from the ideal angle of a perfect tetrahedron (109.47°). Thus, complexes **1–4** show distorted tetrahedral geometries about the cobalt atom, which is also supported by the values calculated for their respective τ_4 parameters, varying between 0.72 and 0.77. As the θ bite angles are in the range $82.5(3)$ – $85.1(7)^{\circ}$, all compounds show an elongated tetrahedral geometry, suggesting that the Co(II) ions possess very large magnetic anisotropies, as observed in similar homoleptic Co(II) complexes encompassing two bidentate chelating ligands reported in the literature.^{7–9,13}

Rajaraman and co-workers²⁴ demonstrated the influence of structural distortions in the values of the zero-field splitting parameters D and E , in several four-coordinate tetrahedral Co(II) complexes. It was revealed that the bite angle θ and the ligands dihedral angle (ϕ) between the two N–Co–N chelation

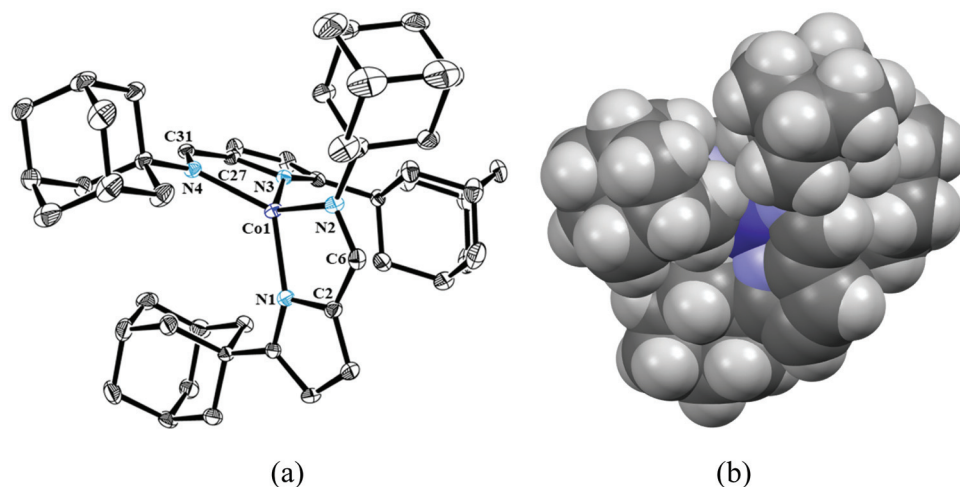


Fig. 1 (a) ORTEP-3 diagram for complex **4** with ellipsoids drawn at 30% probability level. All hydrogen atoms were omitted for clarity. (b) Spacefill view of the X-ray molecular structure of complex **4**, showing the stereochemical protection of the Co(II) metal ion.

Table 1 Bite angles θ , dihedral angles ϕ , interligand angles ω and parameters τ_4 for complexes **1–4**

Complexes	1 ^a		2 ^b	3 ^b	4
	Molecule #1	Molecule #2			this work
Bite angle θ_1 ^c	82.5(3)	83.0(3)	83.8(1)	84.15(7)	84.63(10)
Bite angle θ_2 ^d	82.8(3)	83.4(3)	83.91(14)	85.11(7)	84.8(1)
Dihedral ϕ ^e	81.03(3)	82.00(4)	82.20(17)	84.68(8)	85.2(1)
Angle ω ^f	173.5(2)	174.7(2)	177.12(12)	162.42(5)	170.61(6)
Parameter τ_4 ^g	0.72	0.74	0.74	0.76	0.77

^a Ref. 17. ^b Ref. 18. ^c θ_1 = N1–Co–N2 chelating ligand bite angle. ^d θ_2 = N3–Co–N4 chelating ligand bite angle. ^e ϕ = dihedral angle formed between planes defined by atoms (Co, N1, N2) and (Co, N3, N4). ^f ω = interligand angle formed between dummy bonds Co-centroid (C2–C6) and Co-centroid (C27–C31). ^g Ref. 23.

planes, control the D and E/D values, respectively. In the present family of compounds, the introduction of increasingly bulky groups in the position 5 of the pyrrole ring in complexes 2–4 leads to a slight increase in the ϕ values from 81.03(3) to 85.2(1) (and also of τ_4 from 0.72 to 0.77) (Tables 1 and S2†), meaning that the planes become closer to perpendicularity and, consequently, to a tetrahedral geometry. Despite, the small changes observed, the consequences in the 3d orbitals splitting pattern are visible, indicating significant differences in values of D and E when comparing complex 1 with the remaining complexes 2–4, as shown below in the Theoretical calculations section.

Static (dc) magnetic measurements

Static magnetic susceptibility measurements were performed for complex 4. For complexes 1, 2 and 3 these measurements had already been reported.^{17,18} The $\chi_M T$ versus T plot measured at 500 G in the range of 5–300 K for complex 4 is shown in Fig. 2, where χ_M is the molar magnetic susceptibility per formula unit. The magnetic susceptibility is of 3.28 cm³ K mol⁻¹ at room temperature, corresponding to the expected value for a high spin Co(II), but much higher than the calculated spin-only value for high-spin Co(II), 1.875 cm³ K mol⁻¹ ($S = 3/2$ and $g = 2.00$), indicating a substantial contribution of orbital angular momentum.^{7–10,13,25} Upon decreasing the temperature, the $\chi_M T$ values remain almost constant down to ca. 100 K and then decrease continuously reaching 2.06 cm³ K mol⁻¹ at 5 K. This sudden decrease appears to be due to the presence of a strong axial magnetic anisotropy rather than to intermolecular antiferromagnetic interactions between Co atoms of adjacent molecules in the crystal structure, since their distance is larger than 9 Å.

A comparison of the $\chi_M T$ versus T plot for complex 4 with those of complexes 1–3 is presented in ESI (Fig. S7†). The curves show a similar trend for all compounds. The field dependence of the magnetization, measured at different fixed temperatures showed no hysteresis for all the four complexes

1–4, which can be attributed to QTM or to the slow magnetic sweeping rate of the SQUID magnetometer, which did not allow field sweeping rates larger than about 20 Oe s⁻¹ during measurements (Fig. 2b and S8†). For complex 4, the existence of magnetic anisotropy is also evidenced by the saturation value of 1.95 μ_B at 5 T and 2 K, which is far lower than the theoretical saturation value of 3 μ_B for an isolated Co(II) ion ($g = 2$, $S = 3/2$).

High-frequency EPR (HF-EPR) spectroscopy

To investigate the zero-field splitting and hence to assess the viability of compounds 1–4 as SMMs, we have carried out HF-EPR measurements on all complexes at different frequencies and temperatures (Fig. 3). The spectra of complex 1 at 5 K (Fig. S9†) display one strong, frequency-dependent resonance

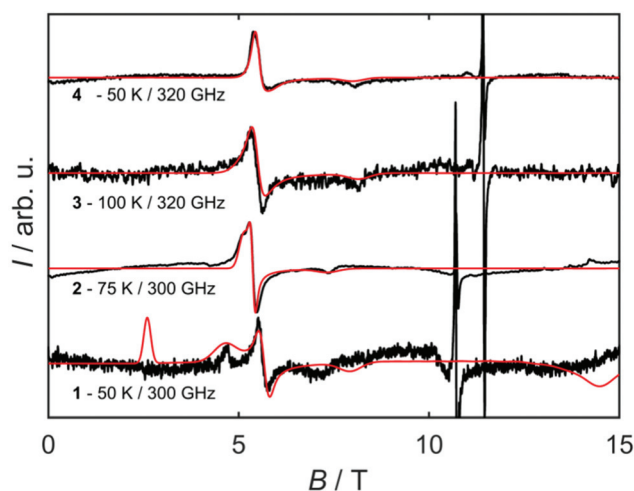


Fig. 3 High-frequency EPR spectra of pressed powder samples of compounds 1–4. Black lines represent the measurement, red lines the simulation on the basis of the spin Hamiltonian parameters given in the text. The strong resonance line at fields higher than 10 T is due to an instrumental artefact.

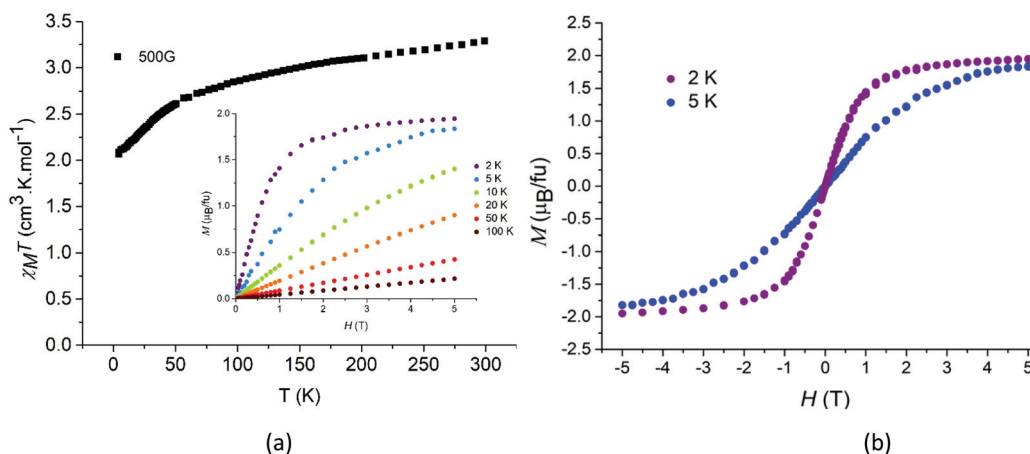


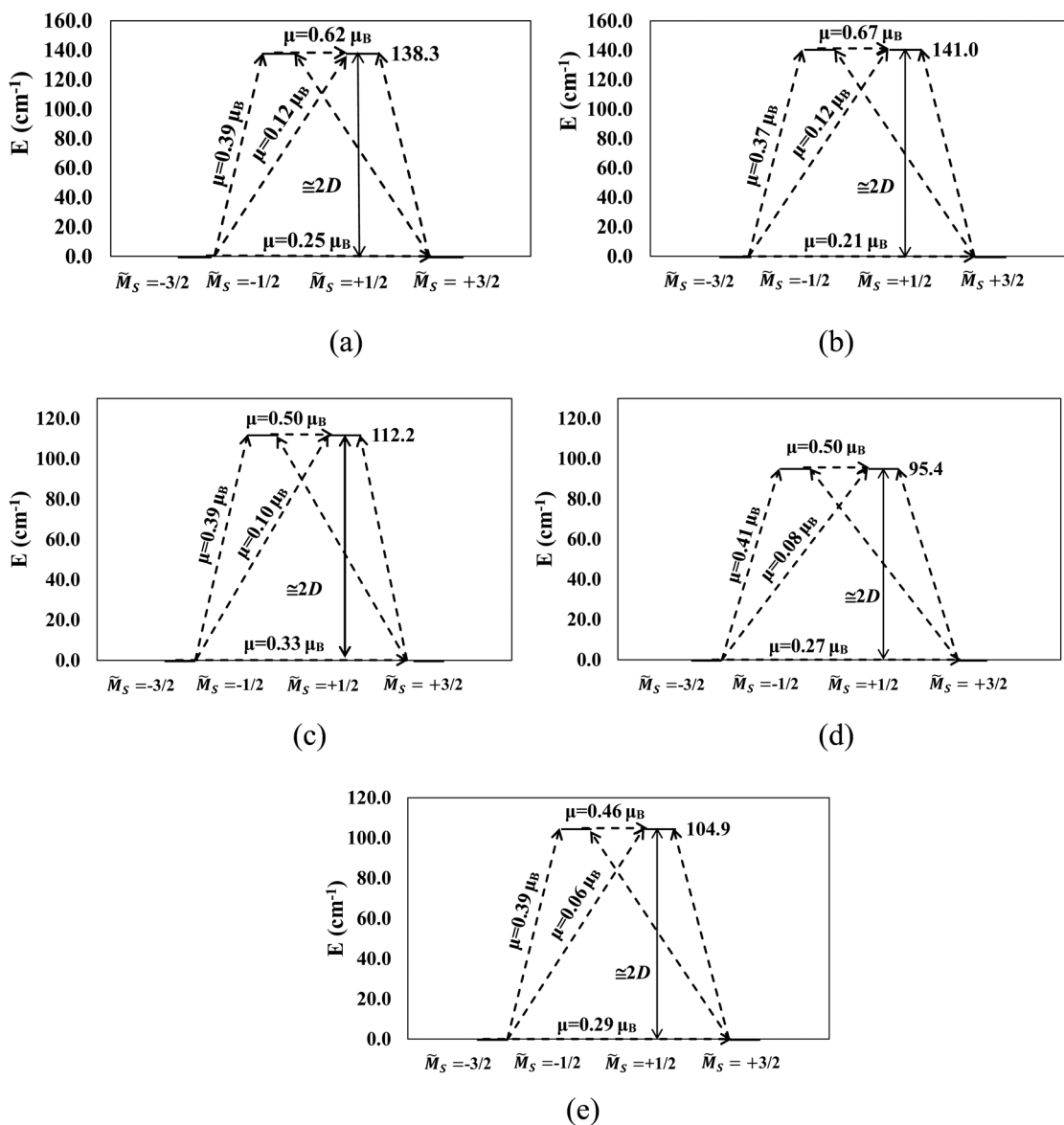
Fig. 2 (a) $\chi_M T$ vs T plot measured at 500 G for complex 4. The inset shows M vs. H at different temperatures. (b) M vs. H plot from 0 to 5 T at 2 and 5 K for complex 4 showing no hysteresis loop at these temperatures.

Table 2 Spin Hamiltonian parameters for compounds 1–4, as derived from SQUID magnetometry and high-frequency EPR

Compound	g -Tensor	D (cm^{-1})	E (cm^{-1})
1	2.05(5), 2.22(2), 2.77(5)	-69(5)	6.5(5)
2	2.05(5), 2.05(5), 2.91(2)	-53(4)	0.85(5)
3	2.10(3), 2.17(3), 2.80(5)	-48(3)	1.0(2)
4	2.00(5), 2.15(5), 2.85 (5)	-52(4)	1.0(2)

line in the $g = 2$ region. Empty sample-holder measurements revealed this resonance line to be an instrumental artefact that was traced to the gold mirror employed. In addition, these spectra show a weak, frequency-dependent upward-pointing resonance line around 3 T for frequencies between 300–375 GHz. This resonance line is attributed to the intra-doublet

transition within the ground Kramers doublet (KD). Its weak intensity, as well as the absence of further resonance lines suggest that the second rank axial zero-field splitting (ZFS) parameter D is large and negative, which is corroborated by the temperature dependence. A further broad feature at around 5 T could not be assigned. Upon increasing the temperature, the intensity of the 3 T resonance line decreases in line with its attribution to a ground state transition (Fig. S10†). At 50 K, further resonance lines become visible in the 5 T region. These lines are attributed to transitions within the excited KD. A fit of the spectra to the spin Hamiltonian $H = \mu_{\text{B}} \mathbf{g} \cdot \hat{\mathbf{S}} + D\hat{S}_z^2 + E(\hat{S}_x^2 - \hat{S}_y^2)$ yielded a slightly rhombic g -tensor (Table 2). The D -value was found to be large and negative ($D = -69 \text{ cm}^{-1}$), which is beneficial for SMM behaviour, and the rhombic ZFS parameter E (transverse anisotropy) is

**Fig. 4** Calculated zero-field splitting plots with transition moments between each spin-orbit state. The two crystallographic units of complex 1 are shown in plots (a) and (b), complex 2 is shown in (c), 3 in (d) and 4 in (e).

less than 10% of the D -value ($E/D = 0.094$) making the ZFS of this system rather axial and thus promising as SMM. HFEPR spectra recorded on a sample of **2** at 5 K display three very weak resonance lines. The lowest-field one is again attributed to the intra-ground-KD transition, and the other two to a minimum amount of solid oxygen trapped in the sample holder.²⁶ At higher temperatures, the resonance line due to the excited KD is clearly observed just above 5 T ($\nu = 300$ GHz, Fig. S11†). Simulations revealed that the g - and D -tensors are even more axial than for **1** (Table 2). Low-temperature HFEPR spectra recorded on samples of **3** and **4** did not show any signal, and higher temperature spectra (Fig. S12–S14†) again displayed resonance lines assigned to the excited KD. The extracted spin Hamiltonian parameters are very similar to those for the other compounds (Table 2). In summary, HFEPR spectroscopy revealed the studied compounds to possess highly axial magnetic anisotropies, with a slight rhombicity in the case of **1**.

The values of D for compounds **2** and **3** previously estimated through the simulation of their static magnetic data¹⁸ are similar to those determined by HFEPR in the present work.

Theoretical calculations

In order to understand the electronic processes at play in these complexes, a multi-reference wavefunction analysis was undertaken employing the Quasi-Degenerate N-Electron Valence Perturbational Theory (QD-NEVPT2) method to reproduce their zero-field splitting and tap into the source of their magnetic anisotropy. A Complete Active Space Self-Consistent Field (CASSCF) calculation was performed over the 3d orbitals totalling 10 quartets and 40 doublets prior to the perturbative step (see computational details).

The most relevant quartet states are briefly summarized in Table S4 (see ESI†).

The calculations were performed on the experimentally determined crystal structures and the corresponding energetics of the KDs and respective transition moments are displayed in Fig. 4. Since complex **1** has two crystallographically distinct units¹⁷ both were treated separately in the calculations.

It may be seen that all the complexes display some measure of QTM with a sizable transition moment between the $\pm 3/2$ components. They are however generally inferior to those with $\Delta M_S \pm 1$. If one defines the best SMM character as the molecule with the largest negative D value this may be observed in complex **1**. The easy axis generally bisects the nitrogen base chelate in this family of complexes (Fig. 5).

The origin of the high ZFS parameter D is predominantly due to the first excited state of quartet multiplicity (represented herein as ${}^4\tilde{A}$ following spectroscopic notation). Indeed, most of the contributions are from quartet states. The magnitude of D is roughly proportional to the highest contribution brought by the ${}^4\tilde{A}$ microstate in every complex (Table 3). Additionally, the largest opposite sign contribution to D originates from the second excited state quartet (${}^4\tilde{B}$). The latter state is also the largest contributor to E . The validity of these results is underlined by the fact that the theoretical values of D , E and g correspond remarkably well to those found in experiment (see Tables 2, 3 and S5†).

To obtain a more intuitive connection between the changes in D and the metal site's ligand field an *Ab Initio* Ligand-Field Theory (AILFT)²⁷ analysis was performed on all the models in their respective magnetic axis frame. This allows for a mapping of the configuration interaction (CI) manifold states into a 3d orbital space (Fig. 6).

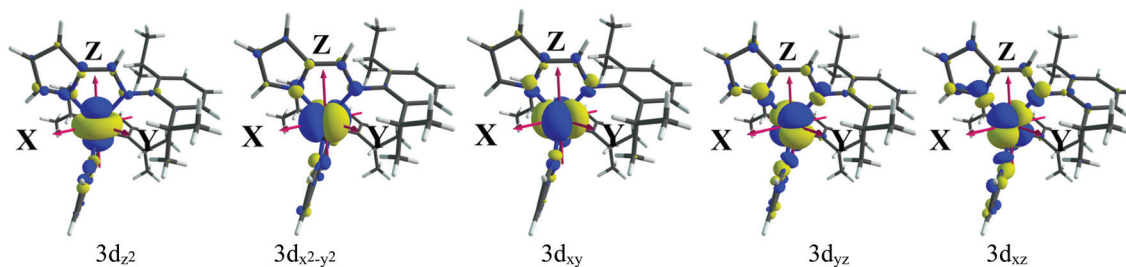


Fig. 5 Active space orbitals of complex **1** shown in their magnetic axis frame.

Table 3 Decomposition of the calculated D and E parameters to second order with corresponding largest contributor states and comparison with experimental values

Complex	D (cm ⁻¹)			E (cm ⁻¹)		
	Calc.	Exp.	Contribution from ${}^4\tilde{A}$ (cm ⁻¹)	Calc.	Exp.	Contribution from ${}^4\tilde{B}$ (cm ⁻¹)
1	-69.8	-69(5)	-88.7 ($d_{xy} \leftarrow d_{x^2-y^2}$)	1.7	6.5(5)	9.8 ($d_{yz} \leftarrow d_{z^2}$)
2	-56.6	-53(4)	-75.0 ($d_{xy} \leftarrow d_{x^2-y^2}$)	1.5	0.85(5)	8.3 ($d_{yz} \leftarrow d_{z^2}$)
3	-47.7	-48(3)	-66.9 ($d_{xy} \leftarrow d_{x^2-y^2}$)	0.9	1.0(2)	8.2 ($d_{yz} \leftarrow d_{z^2}$)
4	-52.4	-52(4)	-71.1 ($d_{xy} \leftarrow d_{x^2-y^2}$)	0.8	1.0(2)	7.8 ($d_{yz} \leftarrow d_{z^2}$)

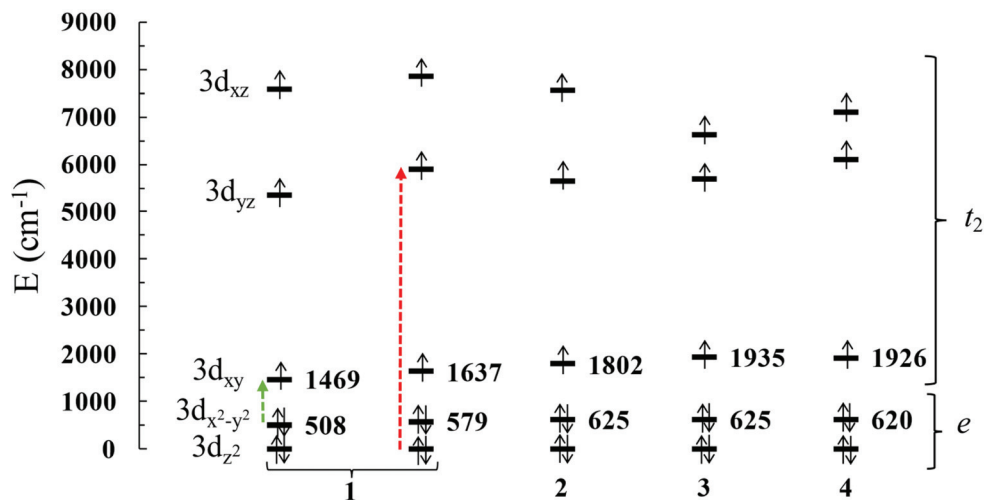


Fig. 6 AILFT-NEVPT2 3d orbital splitting of metal complexes 1–4 with emphasis on the gap between the $3d_{x^2-y^2} \rightarrow 3d_{xy}$ orbitals corresponding to the first excited state.

Since all the complexes are distorted tetrahedra, each of them will split their idealized $e^4(z^2, x^2 - y^2) t_2^3(xy, yz, xz)$ configurations into non-degenerate orbitals, the t_2 set considerably more than e as the former are antibonding orbitals and the latter non-bonding. The $^4\tilde{A}$ quartet corresponds to a single electron transition from the $3d_{x^2-y^2} \rightarrow 3d_{xy}$ orbitals, whereas the $^4\tilde{B}$ state corresponds to $3d_{yz} \rightarrow 3d_{z^2}$. Upon inspection of these respective gaps in all the complexes it is easy to relate the magnitude of the related transition energy Δt_2 with the magnitude of D as the smaller the excitation energy the more negative D will become. Additionally, the degree of ligand admixing in the $3d_{xy}$ molecular orbital is roughly inversely proportional to the negative drop in D . This may be rationalised in terms of the antibonding overlap that raises the energy value of $3d_{xy}$, the energy of $3d_{x^2-y^2}$ staying mostly constant throughout the series. A Löwdin population partitioning of the ligand participation in $3d_{xy}$ for this family of complexes is 2.15%, 2.3%, 2.4% and 2.4% for 1–4, respectively, the corresponding experimental D values being -69 , -53 , -48 and -52 cm^{-1} .

From perturbation theory,^{10,28} the D parameter is related (in D_{2d} point group symmetry) to the gaps between the first quartet electronic states:

$$D \propto \left[\frac{1}{\Delta E(^4\tilde{E} \leftarrow ^4\tilde{B}_1)} - \frac{1}{\Delta E(^4\tilde{B}_2 \leftarrow ^4\tilde{B}_1)} \right] \quad (1)$$

with $^4\tilde{B}_1$ being the ground state term symbol and $^4\tilde{B}_2$ and $^4\tilde{E}$ the first and second excited states, respectively. For the present complexes this can be reduced to:

$$D \propto \left[\frac{1}{\Delta E(^4\tilde{B} \leftarrow ^4\tilde{X})} - \frac{1}{\Delta E(^4\tilde{A} \leftarrow ^4\tilde{X})} \right] = \left[\frac{1}{\Delta E(d_{yz} \leftarrow d_{z^2})} - \frac{1}{\Delta E(d_{xy} \leftarrow d_{x^2-y^2})} \right] \quad (2)$$

These results are in line with those from similar tetrahedral Co(II) SIMs as expounded in the theoretical analysis of Rajaraman and co-workers.²⁴

As structural distortion of the tetrahedral metal site holds the key to optimize the SMM performance of the complexes, it was decided to perform a magnetostructural analysis of a model complex. A Co(II) square planar complex investigated by Carabineiro *et al.*¹⁷ serves as a simple example in this family of homoleptic Co(II) complexes, although employing a (*E*)-2-[*N*-(2,6-bis(isopropyl)phenyl)acetimidino]pyrrolyl ligand, which contains a methyl group substituent of the iminic carbon instead the H atom of complexes 1–4. For the analysis, this ligand was simplified by removing the two isopropyl groups from the phenyl ring and replacing them with hydrogens at a standard bond length.

Two types of distortions were examined with this model: (1) planarization and (2) pyramidalization of the tetrahedron.

In the first instance, it is evident that the switch from tetrahedral to square planar geometry leads to a drop in the D value (Fig. 7a). Eventually upon reaching a square planar geometry (interplanar dihedral angle between the two ligands $\phi < 15^\circ$), the ligand field is high enough for the ground state configuration to change to a doublet in which case there is no ZFS.

The compounds studied in the present work show experimental dihedral angles ϕ in the range of 81.03(3)–85.2(1). In Fig. 7a, this range lies in the most negatively valued region of the model, meaning that the axial anisotropy cannot be much more improved in this way. These results are also typical of other Co(II) tetrahedral complexes as reported by Rajaraman and co-workers.²⁹ Conversely, the E parameter value is very low in the above-mentioned range of experimental dihedral angles (Fig. 7b).

In the second case, the model calculations consisted of monitoring the D value upon sweeping the interligand angle ω , formed between the dummy bonds defined by the Co atom

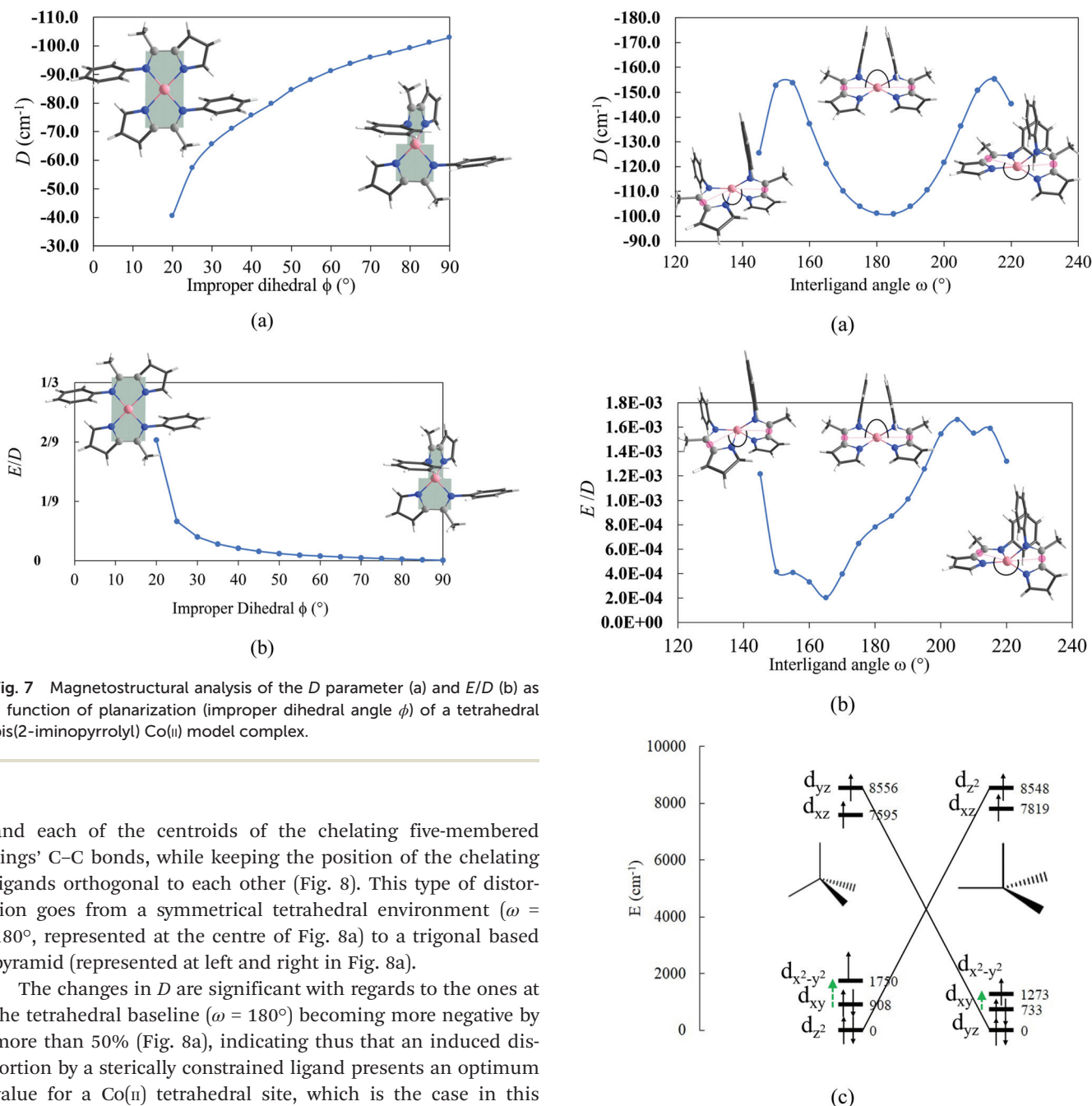


Fig. 7 Magnetostructural analysis of the D parameter (a) and E/D (b) as a function of planarization (improper dihedral angle ϕ) of a tetrahedral bis(2-iminopyrrolyl) Co(II) model complex.

and each of the centroids of the chelating five-membered rings' C-C bonds, while keeping the position of the chelating ligands orthogonal to each other (Fig. 8). This type of distortion goes from a symmetrical tetrahedral environment ($\omega = 180^\circ$, represented at the centre of Fig. 8a) to a trigonal based pyramid (represented at left and right in Fig. 8a).

The changes in D are significant with regards to the ones at the tetrahedral baseline ($\omega = 180^\circ$) becoming more negative by more than 50% (Fig. 8a), indicating thus that an induced distortion by a sterically constrained ligand presents an optimum value for a Co(II) tetrahedral site, which is the case in this family of compounds that present experimental values of angles ω in the range $162.42(5)$ to $177.1(1)^\circ$ (Table 1). This can be explained by a decrease in the $3d_{x^2-y^2} \rightarrow 3d_{xy}$ energy gap from 842 to 540 cm^{-1} in AILFT (Fig. 8c). The E parameter profile is asymmetric, but its absolute value is very small throughout the tested range (Fig. 8b).

Another parameter that can be explored is the ligand bite angle otherwise known as the polar angle θ .²⁴ As these 2-iminopyrrolyl derivatives have two carbon atoms between the coordinating nitrogens, a simple model such as *cis*-[Co(NH₂)₂(NH₃)₂] can be used to account for the changes in D with angular changes. The chemical nature of the ligands is entirely different, but the complex is still isoelectronic with the ones reported in this work. This allows for a quali-

Fig. 8 Magnetostructural analysis of the D parameter (a), E/D (b) and ligand field (c) as a function of angle ω , representing the pyramidalization of a tetrahedral bis(2-iminopyrrolyl) Co(II) model complex (at the centre of (a)). In (a), the dummy atoms used as a reference for the angle value are shown in pink.

tative understanding of the result of the structural changes (Fig. 9).

It may be seen that tetrahedral flattening towards a square planar geometry (symmetrical increase of both θ angles) causes considerable rhombic anisotropy, so much so that the sign of D loses any meaning (Fig. 9a). Upon approaching T_d type symmetry ($\theta = 109.47^\circ$) the sign of D is small and positive,

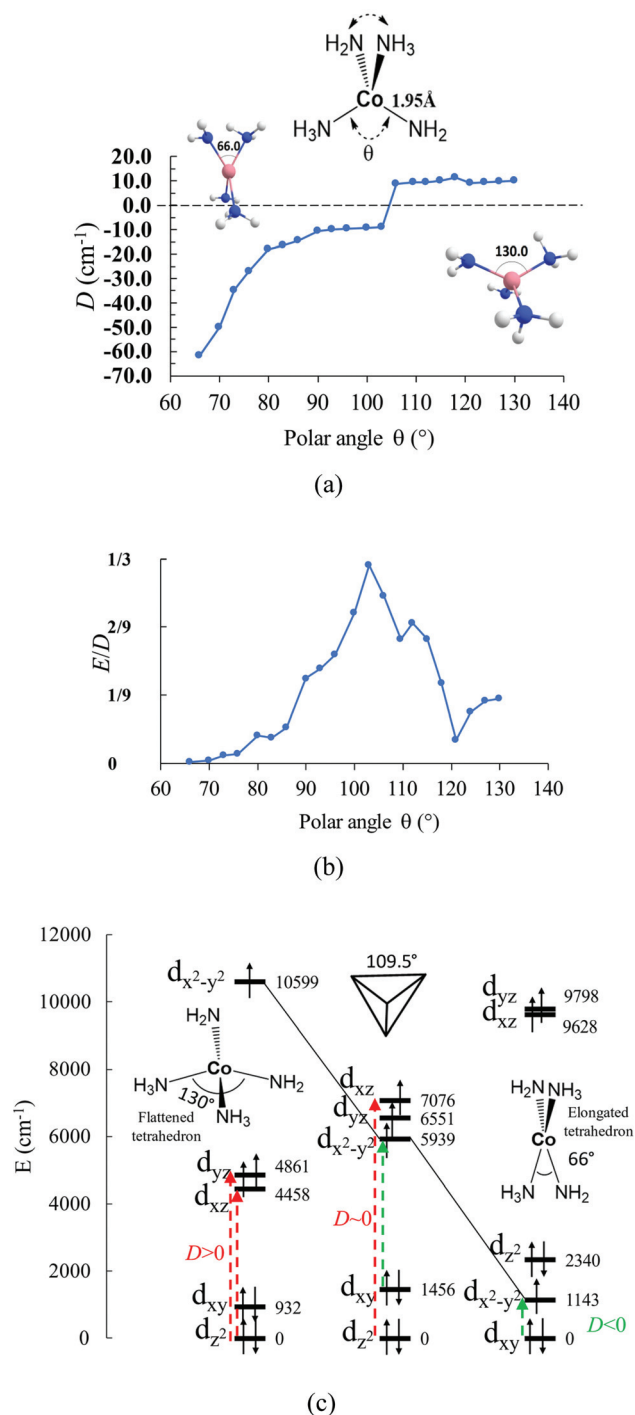


Fig. 9 Variation of the D parameter (a), E/D (b) and ligand field (c) with the ligand bite angle θ .

but as this angle decreases it tends towards zero. At about 85° the system gains axial anisotropy that increases consistently as the bite angle becomes tighter, moreover the rhombic anisotropy parameter E also tends towards zero (Fig. 9b). Because complex **1** displays a more elongated tetrahedral geometry (see experimental values of ligand bite angles θ in Table 1), the values of D are more negative than those calculated for

the remaining compounds 2–4. From an AILFT standpoint, in the flattened tetrahedron geometry (Fig. 9c, left side), the first excited state is multi-configurational largely dominated by two leading configurations: 34% $|(3d_{z^2})^1 (3d_{xy})^2 (3d_{xz})^1 (3d_{yz})^2 (3d_{x^2-y^2})^1|$ and 31% $|(3d_{z^2})^1 (3d_{xy})^2 (3d_{xz})^2 (3d_{yz})^1 (3d_{x^2-y^2})^1|$. This first excited quartet provides the majority contribution with $+12 \text{ cm}^{-1}$ to the D parameter. In the ideal tetrahedral geometry (Fig. 9c, centre), the first excited quartet state is also multiconfigurational with 42% $|(3d_{z^2})^2 (3d_{xy})^1 (3d_{x^2-y^2})^2 (3d_{yz})^1 (3d_{xz})^1|$ and 28% $|(3d_{z^2})^1 (3d_{xy})^2 (3d_{x^2-y^2})^1 (3d_{yz})^1 (3d_{xz})^2|$. In this case, the contribution to D by second order decomposition is $+5.4 \text{ cm}^{-1}$, closer to zero and close to a tipping point from in-plane to axial anisotropy, *i.e.* to potential SMM character. In the extremely compressed model (Fig. 9c, right side), the first excited state is now singly configurational with the occupations $|(3d_{xy})^1 (3d_{x^2-y^2})^2 (3d_{z^2})^2 (3d_{xz})^1 (3d_{yz})^1|$ and a contribution of -76 cm^{-1} to the D parameter.

Due to excessive ligand repulsion and model artifacts, the electron occupations of the ground state of the elongated tetrahedron model are not *aufbau*. Nevertheless, owing to its intrinsic structural rigidity, the bite angle variation in the 2-imino-pyrrolyl chelates is limited to a few degrees, as it can be observed in Table 1 for complexes 1–4 ($82.8(3)$ to $85.2(1)^\circ$), essentially depending on the steric constraints of the coordination sphere. For the compounds under consideration, the bite angle θ is already in the favourable range of axial anisotropy and cannot be much improved.

These results provide hints into improving SMM performance by judicious choice of the geometry of the ligands coordinating the metal site, by consistently shortening the $3d_{x^2-y^2} \rightarrow 3d_{xy}$ gap.

Dynamic (ac) magnetic measurements

Temperature-dependent ac susceptibility measurements at ac magnetic field frequencies from 95 Hz to 9995 Hz were also performed for all the complexes. Apart from complex **1**, all the other compounds 2–4 exhibit a frequency-dependent maximum in the out-of-phase component of the magnetic susceptibility (χ'') in the absence of dc field (Fig. 10a and Fig. S24a, S27a and S32a†).

The lack of signal in complex **1** is caused not only by the occurrence of the QTM process, observed in most of Co(II)-based SIMs,³⁰ but mainly by the presence of a transverse anisotropy (E), in good agreement with the high experimental value of E obtained for **1** in comparison with those of the remaining compounds. For compounds 2–4, although a blocking of the magnetization is observed, the maxima in the out-of-phase component are not well defined, probably due to the presence of fast QTM, which is suppressed by applying a static field. Nevertheless, for complexes 2–4 it was still possible to perform the frequency-dependence measurements at different temperatures in the absence of a dc field (Fig. S28, S33 and S37,† respectively). The study of the field dependence of the ac susceptibility performed at 9 K indicates that the longest relaxation time occurs at approximately at 3000 G for **1**, 1000 G for **2** and 800 G both for **3** and **4**. In fact, as shown in Fig. 10b, for

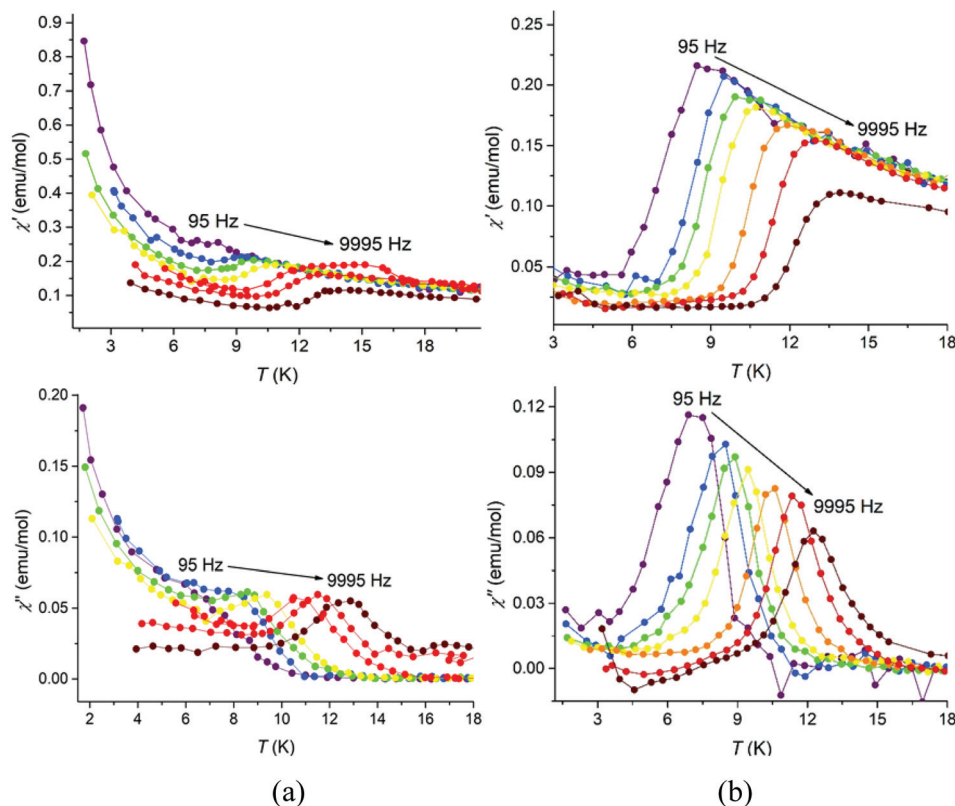


Fig. 10 Temperature-dependence of the in-phase, χ' , and out-of-phase, χ'' , magnetic susceptibilities at several different frequencies indicated for complex **4** under (a) zero static field and (b) 800 G.

compound **4**, and Fig. S24b, S27b and S32b,† for compounds **1**, **2**, and **3**, respectively, the application of such field values significantly enhance the frequency and temperature dependence of the ac susceptibility peaks. Once the optimum field for the slowest relaxation of magnetization was established, the frequency-dependence measurements at different temperatures were carried out in order to determine the different spin relaxation processes involved and calculate the energy barrier, U_{eff} (Fig. 11, for **4**, and Fig. S25, S30 and S35,† for **1**, **2** and **3**, respectively). The Cole–Cole plots (Fig. S26a, S29a/S31a, S34a/S36a and S38,† for **1–4**, respectively) revealed almost perfect semicircle shapes, indicating that only one relaxation process is involved. The resulting data were fitted using a generalized Debye model, where several parameters were obtained such as the relaxation time (τ) and α . The latter is related to the distribution of the relaxation times ($0 \leq \alpha \leq 1$), α being near 0 if only a single relaxation process is present.³¹

The logarithmic τ versus the inverse of the temperature is represented for complex **4** under static dc fields of zero (Fig. 12a) and 800 G (Fig. 12b).

For an ideal SMM, the spin relaxation should occur only through a pure Orbach process, where the energy barrier is determined by a linear fit, using the Arrhenius law: $\tau = \tau_0 \exp(U_{\text{eff}}/kT)$. In the absence of static magnetic field, the fitting parameters effective relaxation barrier and the pre-exponential factor are $U_{\text{eff}} = 51(11) \text{ cm}^{-1}$ with $\tau_0 = 2.2(1) \times 10^{-8} \text{ s}$ for **3**

(Fig. S34b†) and $U_{\text{eff}} = 88(11) \text{ cm}^{-1}$ with $\tau_0 = 1.1(1) \times 10^{-10} \text{ s}$ for complex **4** (Fig. 12a). It also revealed the presence of the QTM mechanism at lower temperatures. As for compound **2**, it was possible to fit the experimental data using eqn (3) with a combination of Orbach and Raman processes, since there is a clear curvature of the $\ln(\tau)$ vs. T^{-1} plot (Fig. S29b†). Under a static magnetic field, the QTM relaxation process is suppressed for all compounds. By using the Arrhenius law, the obtained parameters are $U_{\text{eff}} = 76(4) \text{ cm}^{-1}$ with $\tau_0 = 5.1(3) \times 10^{-9} \text{ s}$ for **1** (Fig. S26b†), $U_{\text{eff}} = 90.6(5) \text{ cm}^{-1}$ with $\tau_0 = 6.0(4) \times 10^{-10} \text{ s}$ for **2** (Fig. S31b†), $U_{\text{eff}} = 88(3) \text{ cm}^{-1}$ with $\tau_0 = 1.5(3) \times 10^{-10} \text{ s}$ for **3** (Fig. S36b†) and $U_{\text{eff}} = 85(4) \text{ cm}^{-1}$ with $\tau_0 = 5.1(4) \times 10^{-10} \text{ s}$ for complex **4** (Fig. 12b). However, the values of the energy barrier are smaller than expected from the energy gap between $M_s = \pm 3/2$ and $M_s = \pm 1/2$, *i.e.* $|2D|$ (138 cm^{-1} for **1**, 106 cm^{-1} for **2**, 96 cm^{-1} for **3** and 104 cm^{-1} for complex **4**), which is also observed for other Co(II) complexes with a similar behaviour. In addition, for all the four complexes there is a clear curvature in the $\ln(\tau)$ vs. T^{-1} plot at lower temperature indicating that other relaxation mechanisms, such as Raman or direct, may be involved. The efforts to include all three mechanisms failed, giving inconsistent values. The best description of the results is obtained by a sum of the Orbach and Raman processes, given by the eqn (3):³²

$$\tau^{-1} = CT^n + \tau_0^{-1} \exp(-U_{\text{eff}}/kT) \quad (3)$$

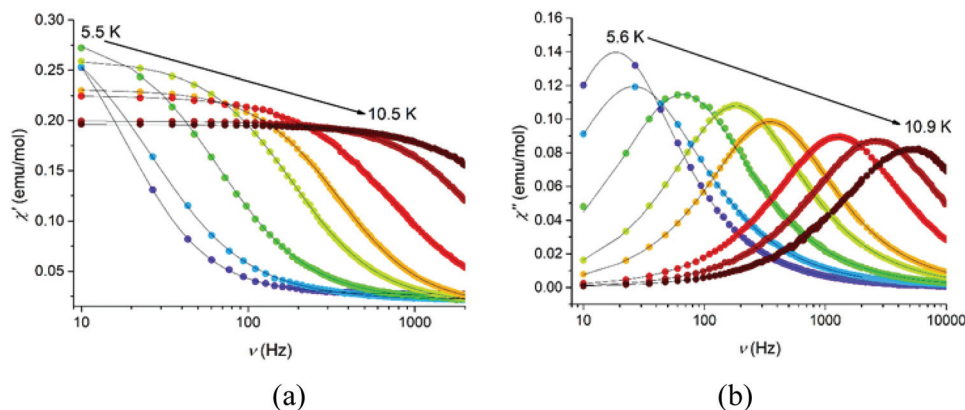


Fig. 11 Frequency-dependence of the (a) in-phase χ' and (b) out-of-phase χ'' magnetic susceptibilities at several different temperatures for complex **4** under a dc field of 800 G. The solid lines are for guidance.

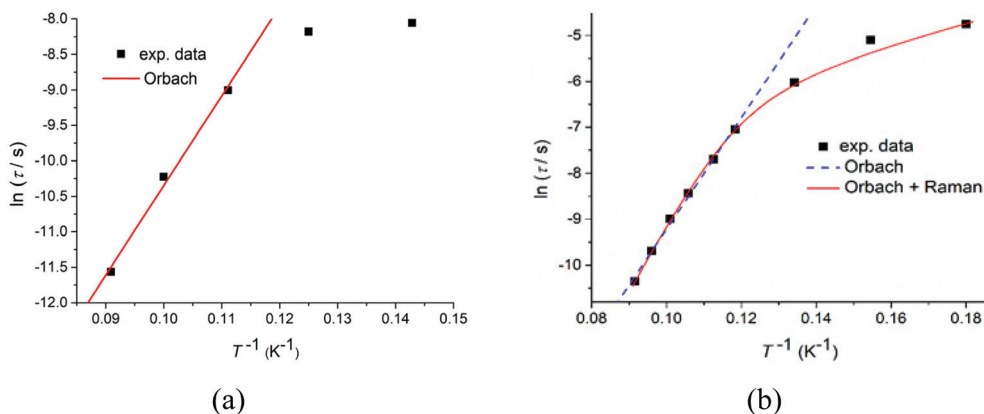


Fig. 12 (a) $\ln(\tau)$ vs. T^{-1} plot for **4** in the absence of an external magnetic field; the red line is the fit for the Orbach process using the Arrhenius law with $U_{\text{eff}} = 88(11) \text{ cm}^{-1}$ and $\tau_0 = 1.1(1) \times 10^{-10} \text{ s}$. (b) $\ln(\tau)$ vs. T^{-1} plot for **4** under 800 G; the red line is the best fit to the sum of Raman and Orbach processes (see eqn (3) in the text) with $C = 0.11(3) \text{ K}^{-n} \text{ s}^{-1}$, $n = 4.1(2)$, $U_{\text{eff}} = 104 \text{ cm}^{-1}$ (fixed) and $\tau_0 = 3.8(1) \times 10^{-11} \text{ s}$ and the blue dash is the fit of the Orbach process using the Arrhenius law with $U_{\text{eff}} = 85(4) \text{ cm}^{-1}$ and $\tau_0 = 5.1(4) \times 10^{-10} \text{ s}$.

where the first and second terms refers to the Raman and Orbach paths, respectively, where C is the Raman coefficient and n the Raman exponent. In Table 4, the calculated parameters obtained from these magnetic relaxation processes fittings are listed.

From eqn (3), and keeping the energy barrier parameter fixed, these results suggest that this system of tetracoordinate Co(II) complexes shows different magnetic behaviours depending on the temperature range, with a clear dominance of the

Orbach process at higher temperatures. However, as the temperature decreases, the Raman mechanism becomes dominant.

Conclusions

In the present work four distorted tetrahedral homoleptic Co(II) complexes containing bidentate N,N' -2-formiminopyrrolyl ligands with increasing steric features are shown to behave as SIMs. From the static magnetic measurements, HF-EPR measurements and theoretical studies all compounds **1–4** present high easy axis magnetic anisotropy, as a result of tetrahedral elongations imposed by the chelating geometry of the 2-iminopyrrolyl ligands. The more elongated structure (smaller values of the bite angle θ) and the slight decreasing covalency in the metal–ligand bond for complex **1** are the main factors for the increase of zero-field splitting parameter (D) when compared to the remaining compounds **2–4**, leading to a smaller gap between the filled $3d_{x^2-y^2}$ orbital and the singly occupied

Table 4 Orbach and Raman relaxation parameters for complexes **1–4**

Parameters	Complex 1	Complex 2	Complex 3	Complex 4
H_{dc} (G)	3000	1000	800	800
C ($\text{K}^{-n} \text{ s}^{-1}$)	0.086(9)	0.02(3)	0.021(4)	0.11(3)
n	4.86(5)	4.9(7)	5.4(1)	4.1(2)
U_{eff} (cm^{-1})	138	106	96	104
τ_0 (s)	$1.14(6) \times 10^{-11}$	$1.3(2) \times 10^{-10}$	$6.8(2) \times 10^{-11}$	$3.8(1) \times 10^{-11}$

$3d_{xy}$ orbital. However, the substitutions in the second coordination sphere (in the position 5 of the pyrrolyl ring) with bulky groups in compounds 2–4 revealed to be beneficial, despite the lower values of D obtained. For complex 1, the calculated parameters g and E , by HFEPR and *ab initio* calculations, showed a pronounced transverse magnetic anisotropy (E), which led to differences in the magnetic properties of this compound.

The dynamic ac magnetic measurements revealed that complexes 2–4 exhibit SIM behaviour in the absence of an external magnetic field, whereas this important feature is not observed for complex 1. This is assigned to the higher values of E in complex 1, which triggers the QTM process rather than the thermally assisted Orbach relaxation mechanism. In addition to the lack of signal under zero static magnetic field, a much higher field is required to overcome the QTM process in complex 1. The energy barriers (U_{eff}) are considerably high for all the compounds studied, because of the occurrence of two relaxation processes: Raman mechanism, at low temperatures, and Orbach mechanism, at higher temperatures. The U_{eff} values in this family of complexes are higher than the majority of tetracoordinated Co(II)-based SIMs found in the literature, revealing them as very promising systems.

Presently, we are still challenged by the steric limits of the 2-iminopyrrolyl framework, and whether it is synthetically possible to employ a chelating ligand of this family bulkier than that of complex 4, while maintaining a stable 1:2 Co:ligand stoichiometry ratio (*i.e.* [Co(2-iminopyrrolyl)₂]), and to further evaluate its impact in the SIM behaviour of this system. We are also studying modifications in the 2-iminopyrrolyl ligand, such as the use of electron-withdrawing or -donating substituents, or the induction of further asymmetry in this ligand set, which may lead to more favourable distortions of the cobalt tetrahedral geometry toward a clear enhancement of the SIM properties of this family of complexes.

Experimental section

General considerations

All operations dealing with air- and/or moisture-sensitive materials were carried out under inert atmosphere using a dual vacuum/nitrogen line, glovebox and standard Schlenk techniques.³³ All solvents used were pre-dried with 4 Å molecular sieves and purified by refluxing over a suitable drying agent followed by distillation under nitrogen. THF was dried over sodium/benzophenone and *n*-hexane over calcium hydride. Solvents and solutions were transferred using a positive pressure of nitrogen through stainless steel cannulas and mixtures were filtered in a similar way using modified cannulas that could be fitted with glass fiber filter disks. The remaining reagents were used as received from commercial sources, namely 1-adamantyl chloride (Alfa Aesar) and 1-adamantylamine (Alfa Aesar). 2-(1-Adamantyl)-1*H*-pyrrole was prepared as described in the literature.¹⁹

Elemental analyses were performed in a Fisons Instrument Mod EA-1108, at Laboratório de Análises (IST).

FTIR measurements were conducted on a Bruker Alpha II ATR IR spectrometer located inside a glovebox.

Nuclear magnetic resonance (NMR) measurements

The NMR spectra of the ligand precursor II and complex 4 were recorded on a Bruker Avance III 300 (¹H, 300.130 MHz; ¹³C, 75.468 MHz) spectrometer. The spectra were referenced internally using the residual protio-solvent (¹H) or solvent (¹³C) resonances, and are reported relative to tetramethylsilane ($\delta = 0$). For compounds stable in air- and/or moisture, the samples were dissolved in CDCl₃ and prepared in common NMR tubes. Complex 4 was dissolved in degassed and dried C₆D₆ or toluene-*d*₈, with the corresponding solution being prepared in a J. Young tube, in a glovebox. The deuterated solvents were dried over activated 4 Å molecular sieves and degassed by the freeze-pump-thaw technique. The magnetic susceptibility measurements in solution were carried out by the Evans method,²¹ using a 3% solution of hexamethyldisiloxane in toluene-*d*₈ as reference. All resonances were characterized by their chemical shifts (δ), quoted in ppm. Multiplicities were abbreviated as follows: broad (br), singlet (s) and multiplet (m).

Synthesis of the ligand precursor II and complex 4

Synthesis of 5-(1-adamantyl)-2-formylpyrrole (I). The reaction was adapted from a procedure described in the literature involving Vilsmeier-Haack acylation conditions.²⁰ The Vilsmeier reagent was prepared by adding dropwise a toluene solution (15 mL) of POCl₃ (4 mL, 41.8 mmol) to an ice-cooled solution of *N,N*-dimethylformamide (3.3 mL, 41.8 mmol) in toluene (15 mL), under nitrogen. After stirring for 30 minutes at room temperature, the resulting product was cooled and a solution of the 2-(1-adamantyl)-1*H*-pyrrole (7 g, 34.8 mmol) in toluene (120 mL) was added dropwise. The reaction mixture was allowed to warm up to room temperature and left stirring overnight. A water-ice mixture was added followed by the addition of NaHCO₃ powder to reach pH = 7. An aqueous solution of NaOH was also added until pH = 12. The mixture stirred for 1 hour and then the organic layer was extracted with CHCl₃, dried with MgSO₄ and all the volatile materials were removed under vacuum. The resulting oil was washed with *n*-hexane and dried under vacuum to afford a brown powder of I. Yield: 6.8 g (86%).

¹H NMR (300 MHz, CDCl₃): δ 9.61 (br, 1H, NH), 9.38 (s, 1H, O=CH), 6.89 (br, 1H, H3 *pyrr*), 6.09 (br, 1H, H4 *pyrr*), 2.07 (m, 3H, 1-Ad CH), 1.92 (m, 6H, 1-Ad CH₂), 1.76 (m, 6H, 1-Ad CH₂). ¹³C{¹H} NMR (75 MHz, CDCl₃): δ 178.4 (O=CH), 162.4 (1-Ad C), 152.1 (C5 *pyrr*), 131.6 (C2 *pyrr*), 122.4 (C3 *pyrr*), 106.6 (C4 *pyrr*), 42.2 (1-Ad CH₂), 36.6 (1-Ad CH₂), 28.4 (1-Ad CH). Anal. calc. for C₁₅H₁₉NO·0.02CHCl₃: C, 77.85; H, 8.28; N, 6.05. Found: C, 77.90; H, 8.54; N, 6.16.

Synthesis of 5-(1-adamantyl)-2-(*N*-(1-adamantyl)formimino)pyrrole (II). To a solution of 5-(1-adamantyl)-2-formylpyrrole (2.53 g; 11.0 mmol) in toluene (50 mL) was added 1-adamanty-

lamine (1.66 g; 11.0 mmol) and a catalytic amount of *p*-toluenesulfonic acid (0.040 g; 0.21 mmol). The mixture was left to reflux for 64 hours. After cooling to room temperature, the solvent was removed under vacuum, washed with *n*-hexane and extracted with diethyl ether. The solution was concentrated and stored at $-20\text{ }^{\circ}\text{C}$ to afford a light brown powder of **II**. Yield: 2.14 g (60%).

^1H NMR (300 MHz, CDCl_3): δ 7.96 (s, 1H, $\text{N}=\text{CH}$), 6.37 (br, 1H, H3 *pyrr*), 5.95 (br, 1H, H4 *pyrr*), 5.79 (br, 1H, *NH*), 2.21–1.66 (m, 30H, 5-(1-Ad) + N-(1-Ad)). $^{13}\text{C}\{^1\text{H}\}$ NMR (75 MHz, CDCl_3): δ 146.0 ($\text{N}=\text{CH}$), 122.0 (C5 *pyrr*), 114.5 (C2 *pyrr*), 106.5 (C3 *pyrr*), 103.9 (C4 *pyrr*), 43.3 (1-Ad CH_2), 42.6 (1-Ad CH_2), 36.7 (1-Ad CH_2), 36.6 (1-Ad CH_2), 29.7 (1-Ad CH), 28.5 (1-Ad CH). Anal. calc. for $\text{C}_{25}\text{H}_{34}\text{N}_2\cdot 0.9\text{C}_4\text{H}_{10}\text{O}$: C, 80.01; H, 10.10; N, 6.53. Found: C, 79.89; H, 9.85; N, 6.45.

$[\text{Co}\{\kappa^2\text{N},\text{N}'\text{-5-(1-adamantyl)-NC}_4\text{H}_2\text{-2-C(H)=N(1-adamantyl)}\}_2]$
(**4**)

NaH (0.041 g, 1.7 mmol) was suspended in THF (20 mL) and a THF (20 mL) solution of the ligand precursor **II** (0.54 g, 1.5 mmol) was added. The mixture was allowed to stir for 2 hours, at $90\text{ }^{\circ}\text{C}$, under nitrogen, yielding a brown-red suspension. After cooling to room temperature, the solution was filtered and added dropwise to a suspension of anhydrous CoCl_2 (0.097 g, 0.75 mmol) in THF (10 mL), which was cooled to $-78\text{ }^{\circ}\text{C}$. The mixture was allowed to warm up to room temperature while stirring overnight. All volatiles were evaporated under reduced pressure, and the residue was extracted with *n*-hexane until extracts were colourless. The solution was concentrated and stored at $-20\text{ }^{\circ}\text{C}$, from which red crystals of **4** suitable for X-ray diffraction were obtained. Yield: 0.41 g (69%).

^1H NMR (300 MHz, C_6D_6): δ 116.36 (br), 30.43 (br), 0.07 (br), -6.50 , -7.07 , -7.81 (br), -10.35 (br), -14.23 , -16.18 (br), -47.45 , -55.95 (br). Anal. calc. for $\text{C}_{50}\text{H}_{66}\text{CoN}_4$: C, 76.79; H, 8.51; N, 7.16. Found: C, 76.56; H, 8.55; N, 6.87. μ_{eff} (toluene- d_8) = $4.7\mu_{\text{B}}$. FTIR (ATR, cm^{-1}): 1566 (s, $\text{C}=\text{N}$).

Powder X-ray diffraction

The samples used were ground with a mortar and pestle inside the glove-box and subsequently, mounted on a silicon plate within a PERSPEX sample holder that could be fitted with an air-tight lid. Data were collected in a D8 Advance Bruker AXS θ - 2θ diffractometer, with a copper radiation source ($\text{Cu K}\alpha$, $\lambda = 1.5406\text{ \AA}$) and secondary monochromator, operated at 40 kV and 30 mA. The Mercury 2020.3.0 software was used for the calculation of X-ray powder diffraction patterns on the basis of the single crystal structure determinations. Comparison of the calculated and observed X-ray powder diffraction patterns was carried out for all the complexes **1–4** (see Fig. S3–S6 in ESI†).

Single crystal X-ray diffraction

Crystals of **4** were covered with polyfluoroether oil, selected under an inert atmosphere, and mounted on a nylon loop. The crystallographic data were collected using graphite monochromated $\text{Mo-K}\alpha$ radiation ($\lambda = 0.71073\text{ \AA}$) on a Bruker AXS-KAPPA

APEX II diffractometer equipped with an Oxford Cryosystem open-flow nitrogen cryostat, at 150 K. Cell parameters were retrieved using Bruker SMART software and refined using Bruker SAINT³⁴ on all observed reflections. Absorption corrections were applied using SADABS.³⁵ Structure solution and refinement were performed using direct methods with the programs SIR2014³⁶ and SHELXL³⁷ included in the package of programs WINGX-Version 2014.1.³⁸ All non-hydrogen atoms were refined anisotropically and the hydrogen atoms were inserted in idealized positions and refined as riding on the parent carbon atom. All the structures refined to a perfect convergence. The graphic presentation was generated using ORTEP-3,³⁹ where ellipsoids were drawn with a 30% probability, and the hydrogen atoms were omitted for clarity; Mercury 2020.3.0 software was used for the generation the spacefill representation in Fig. 1b. Data was deposited in CCDC under the deposit number 2160416 for **4**.†

HFEPN spectroscopy

The spectra were recorded between 300 and 375 GHz, 0–15 T and 5–210 K on a home-built spectrometer consisting of a VDI signal generator, VDI broadband frequency multipliers, a Thomas Keating Ltd quasioptical bridge and probe, and a QMC Instruments InSb bolometer detector.⁴⁰ The samples were mounted in a 15 T Oxford Instruments helium bath magnetocryostat. The external field is modulated at kHz frequencies to allow for lock-in detection.

Computational studies

The ORCA program⁴¹ package version 4.2.1 was used for all the property calculations using the structures derived from single crystal X-ray diffraction as input. The N-Electron Valence perturbational method^{42,43} to second order was employed with the Resolution of Identity⁴⁴ (RI-NEVPT2) approximation. The Complete Active Space Self-Consistent Field (CASSCF)⁴⁵ wavefunction was determined in the full configuration interaction (CI) space as the state-average of 10 quartets and 40 doublets (seven electrons in five 3d orbitals). The single state perturbed NEVPT2 wavefunctions underwent a multi-state extension to quasi-degenerate NEVPT2 (QD-NEVPT2)⁴⁶ in the Nakano⁴⁷ formulation.

The exchange integrals were calculated through the RIJCOSX^{48,49} density fitting technique with 5 accuracy points (GridX5).

The Douglas-Kroll-Hess^{50–52} scalar relativistic Hamiltonian truncated to second order (DKH2) was applied with the correspondingly contracted triple zeta polarized basis sets (DKH-TZVP) for all the elements except hydrogen, the latter having been assigned a split-valence basis set (DKH-SVP). The density fitting auxiliary basis sets were chosen to be the generic Karlsruhe⁵³ def2-TZVP/C specific basis set for the treatment of the perturbative RI section in addition to the segmented relativistically contracted (SARC/J) set⁵⁴ for the non-perturbative Coulomb integrals.

The anisotropy (*D*, *E*) parameters and *g* values were calculated in the framework of QD-NEVPT2 *via* the spin-orbit mean

field^{55,56} formalism using an effective Hamiltonian⁵⁷ by projection of the CI matrix onto the model states. The spin orbit states were projected onto the giant spin Hamiltonian:

$$\hat{H} = \hat{S}\mathbf{D}\hat{S} \quad (4)$$

where \mathbf{D} is the zero-field splitting tensor possessing the following scalar parameters in the magnetic axis frame: $D = 3/2D_{zz}$ and $E = (D_{xx} - D_{yy})/2$. By convention $D_{xx} \geq D_{yy}$ so that E is always positive. If $D < 0$ there may be a barrier for magnetization reversal ($-M_s \rightarrow +M_s$), whereas for $D > 0$ there can be no magnetization reversal and the spin aligns itself in the xy plane.

Magnetic measurements

All the samples (10–20 mg) used in the magnetic measurements were transferred to the sample holder in a glovebox, due to their air sensitivity.

The static (dc) magnetic measurements were performed using a 6.5 T S700X SQUID (Cryogenic Ltd) magnetometer. The magnetic susceptibility was measured as a function of temperature under a static magnetic field of 500 G in the temperature range of 5–300 K. The magnetization curves were also obtained from 0 to 5 T at different temperatures (2, 5, 10, 20, 50 and 100 K). The diamagnetism correction for the experimental data was estimated using the Pascal constants as -3.5×10^{-4} , -4.4×10^{-4} , -4.9×10^{-4} and -5.1×10^{-4} emu mol⁻¹ for compounds **1**, **2**, **3** and **4**, respectively.⁵⁸

The dynamic (ac) magnetic measurements were performed using a MagLab 2000 (Oxford Instruments) for complexes **2** and **4** and a Vibrating Sample Magnetometer, VSM (Cryogenic Ltd) for complexes **1** and **3**. The temperature dependence of the in-phase and out-of-phase magnetic susceptibilities were studied at different frequencies from 95 up to 5000 Hz under zero dc field and an applied field (3000 G for **1**, 1000 G for **2** and 800 G for **3** and **4**). The frequency dependence of the ac susceptibility was performed at several different temperatures from 5 K to 15 K under an applied dc field (3000 G for **1**, 1000 G for **2** and 800 G for **3** and **4**).

Conflicts of interest

There are no conflicts of interest to declare.

Acknowledgements

We thank Dr Auguste Fernandes and Prof. M. Teresa Duarte for performing the powder X-ray diffraction analysis. We thank the Fundação para a Ciência e a Tecnologia for financial support (Projects PTDC/QUI-QIN/31585/2017 and PTDC/QUI-QFI/29236/2017) and for a fellowship to P.S.F. (PD/BD/135530/2018 – ChemMat PhD Program). Centro de Química Estrutural (CQE) and Institute of Molecular Sciences (IMS), Centro de Ciências e Tecnologias Nucleares (C²TN) and BioISI – Biosystems & Integrative Sciences Institute acknowledge the

financial support of Fundação para a Ciência e Tecnologia (respectively: Projects UIDB/00100/2020, UIDP/00100/2020 and LA/P/0056/2020; UIDB/04349/2020, UIDP/04349/2020 and LISBOA-01-0145-FEDER-022096; and UIDB/04046/2020 and UIDP/04046/2020). J.v.S., and D.H. thank the Landesgraduiertenförderung Baden-Württemberg and the German Science Foundation DFG (SL104/10).

References

- R. Sessoli, D. Gatteschi, A. Caneschi and M. A. Novak, Magnetic bistability in a metal-ion cluster, *Nature*, 1993, **365**, 141–143.
- M. Fondo, A. Escuer and J. M. Herrera, Molecular Magnets, *Front. Chem.*, 2019, **7**, 229.
- J. P. Launay and M. Verdaguer, *Electrons in Molecules: From Basic Principles to Molecular Electronics*, Oxford University Press, 2013, p. 130.
- M. J. Aubin, Z. Sun, H. J. Eppley, E. M. Rumberger, I. A. Guzei, K. Folting, P. K. Gantzel, A. L. Rheingold, G. Christou and D. N. Hendrickson, Single-Molecule Magnets: Jahn–Teller Isomerism and the Origin of Two Magnetization Relaxation Processes in Mn12 Complexes, *Inorg. Chem.*, 2001, **40**, 2127–2146.
- F. Neese and D. A. Pantazis, What is not required to make a single molecule magnet, *Faraday Discuss.*, 2011, **148**, 229–238.
- G. A. Craig and M. Murrie, 3d single-ion magnets, *Chem. Soc. Rev.*, 2015, **44**, 2135–2147.
- J. M. Zadrozny and J. R. Long, Slow Magnetic Relaxation at Zero Field in the Tetrahedral Complex [Co(SPh)₄]²⁻, *J. Am. Chem. Soc.*, 2011, **133**, 20732–20734.
- J. M. Zadrozny, J. Telser and J. R. Long, Slow magnetic relaxation in the tetrahedral cobalt(II) complexes [Co(EPh)₄]²⁻ (E = O, S, Se), *Polyhedron*, 2013, **64**, 209–217.
- M. S. Fataftah, J. M. Zadrozny, D. M. Rogers and D. E. Freedman, A Mononuclear Transition Metal Single-Molecule Magnet in a Nuclear Spin-Free Ligand Environment, *Inorg. Chem.*, 2014, **53**, 10716–10721.
- Y. Rechkemmer, F. D. Breitgoff, M. van der Meer, M. Atanasov, M. Hakl, M. Orlita, P. Neugebauer, F. Neese, B. Sarkar and J. van Slageren, A four-coordinate cobalt(II) single-ion magnet with coercivity and a very high energy barrier, *Nat. Commun.*, 2016, **7**, 10467.
- E. Carl, S. Demeshko, F. Meyer and D. Stalke, Triimidosulfonates as Acute Bite-Angle Chelates: Slow Relaxation of the Magnetization in Zero Field and Hysteresis Loop of a CoII Complex, *Chem. – Eur. J.*, 2015, **21**, 10109–10115.
- J. Vallejo, E. Pardo, M. Viciano-Chumillas, I. Castro, P. Amorós, M. Déniz, C. Ruiz-Pérez, C. Yuste-Vivas, J. Krzystek, M. Julve, F. Lloret and J. Cano, Reversible Solvatomagnetic Switching in a Single-Ion Magnet from an Entatic State, *Chem. Sci.*, 2017, **8**, 3694–3702.

- 13 H. Cui, F. Lu, X. Chen, Y. Zhang, W. Tong and Z. Xue, Zero-Field Slow Magnetic Relaxation and Hysteresis Loop in Four-Coordinate Co^{II} Single-Ion Magnets with Strong Easy-Axis Anisotropy, *Inorg. Chem.*, 2019, **58**, 12555–12564.
- 14 (a) R. M. Bellabarba, P. T. Gomes and S. I. Pascu, Synthesis of allyl- and aryl-iminopyrrolyl complexes of nickel, *Dalton Trans.*, 2003, 4431–4436; (b) T. F. C. Cruz, P. S. Lopes, L. C. J. Pereira, L. F. Veiros and P. T. Gomes, Hydroboration of Terminal Olefins with Pinacolborane Catalyzed by New Mono(2-Iminopyrrolyl) Cobalt(II) Complexes, *Inorg. Chem.*, 2018, **57**, 8146–8159; (c) T. F. C. Cruz, L. F. Veiros and P. T. Gomes, Cobalt(I) Complexes of 5-Aryl-2-iminopyrrolyl Ligands: Synthesis, Spin Isomerism, and Application in Catalytic Hydroboration, *Inorg. Chem.*, 2018, **57**, 14671–14685; (d) C. A. Figueira, P. S. Lopes, C. S. B. Gomes, J. C. S. Gomes, F. Lemos and P. T. Gomes, New Phenyl-nickel Complexes of Bulky 2-Iminopyrrolyl Chelates: Synthesis, Characterisation and Application as Aluminium-free Catalysts for the Production of Hyperbranched Polyethylene, *Dalton Trans.*, 2018, **47**, 15857–15872; (e) C. A. Figueira, P. S. Lopes, C. S. B. Gomes, J. C. S. Gomes, L. F. Veiros, F. Lemos and P. T. Gomes, Neutral Mono(5-aryl-2-iminopyrrolyl)nickel(II) Complexes as Precatalysts for the Synthesis of Highly Branched Ethylene Oligomers: Preparation, Molecular Characterization, and Catalytic Studies, *Organometallics*, 2019, **38**, 614–625; (f) T. F. C. Cruz, L. C. J. Pereira, J. C. Waerenborgh, L. F. Veiros and P. T. Gomes, Hydroboration of Terminal Olefins With Pinacolborane Catalyzed by New 2-Iminopyrrolyl Iron(II) Complexes, *Catal. Sci. Technol.*, 2019, **9**, 3347–3360; (g) T. F. C. Cruz, C. A. Figueira, L. F. Veiros and P. T. Gomes, Benzylnickel(II) Complexes of 2-Iminopyrrolyl Chelating Ligands: Synthesis, Structure, and Catalytic Oligo-/Polymerization of Ethylene to Hyperbranched Polyethylene, *Organometallics*, 2021, **40**, 2594–2609; (h) T. F. C. Cruz, P. S. Lopes and P. T. Gomes, Allylnickel(II) complexes of bulky 5-substituted-2-iminopyrrolyl ligands, *Polyhedron*, 2021, **207**, 115357; (i) T. F. C. Cruz, L. F. Veiros and P. T. Gomes, Hydrosilylation of Aldehydes and Ketones Catalyzed by a 2-Iminopyrrolyl Alkyl-manganese(II) Complex, *Inorg. Chem.*, 2022, **61**, 1195–1206.
- 15 (a) C. S. B. Gomes, D. Suresh, P. T. Gomes, L. F. Veiros, M. T. Duarte, T. G. Nunes and M. C. Oliveira, Sodium complexes containing 2-iminopyrrolyl ligands: the influence of steric hindrance in the formation of coordination polymers, *Dalton Trans.*, 2010, **39**, 736–748; (b) D. Suresh, C. S. B. Gomes, P. T. Gomes, R. E. Di Paolo, A. L. Maçanita, M. J. Calhorda, A. Charas, J. Morgado and M. T. Duarte, Syntheses and photophysical properties of new iminopyrrolyl boron complexes and their application in efficient single-layer non-doped OLEDs prepared by spin coating, *Dalton Trans.*, 2012, **41**, 8502–8505; (c) D. Suresh, P. S. Lopes, B. Ferreira, C. A. C. Figueira, C. S. B. Gomes, P. T. Gomes, R. E. Di Paolo, A. L. Maçanita, M. T. Duarte, A. Charas, J. Morgado and M. J. Calhorda, Tunable Fluorophores based on 2-(N-Arylimino)pyrrolyl Chelates of Diphenylboron: Synthesis, Structure, Photophysical Characterization and Application in OLEDs, *Chem. – Eur. J.*, 2014, **20**, 4126–4140; (d) D. Suresh, C. S. B. Gomes, P. L. Lopes, C. A. C. Figueira, B. Ferreira, P. T. Gomes, R. E. Di Paolo, A. L. Maçanita, M. T. Duarte, A. Charas, J. Morgado, D. Vila-Viçosa and M. J. Calhorda, Luminescent Di- and Trinuclear Boron Complexes Based on Aromatic Iminopyrrolyl Spacer Ligands: Synthesis, Characterization and Application in OLEDs, *Chem. – Eur. J.*, 2015, **21**, 9133–9149; (e) D. Suresh, B. Ferreira, P. S. Lopes, C. S. B. Gomes, P. Krishnamoorthy, A. Charas, D. Vila-Viçosa, J. Morgado, M. J. Calhorda, A. L. Maçanita and P. T. Gomes, Boron complexes of aromatic ring fused iminopyrrolyl ligands: synthesis, structure, and luminescence properties, *Dalton Trans.*, 2016, **45**, 15603–15620; (f) P. Krishnamoorthy, B. Ferreira, C. S. B. Gomes, D. Vila-Viçosa, A. Charas, J. Morgado, M. J. Calhorda, A. L. Maçanita and P. T. Gomes, Violet-blue emitting 2-(N-alkylimino)pyrrolyl organoboranes: Synthesis, structure and luminescent properties, *Dyes Pigm.*, 2017, **140**, 520–532; (g) A. I. Rodrigues, C. A. Figueira, C. S. B. Gomes, D. Suresh, B. Ferreira, R. E. Di Paolo, M. J. Calhorda, D. de Sá Pereira, F. B. Dias, J. Morgado, A. L. Maçanita and P. T. Gomes, Boron complexes of aromatic 5-substituted iminopyrrolyl ligands: synthesis, structure, and luminescence properties, *Dalton Trans.*, 2019, **48**, 13337–13352; (h) A. I. Rodrigues, P. Kishnamoorthy, C. S. B. Gomes, N. Carmona, R. E. Di Paolo, P. Panda, J. Pina, J. S, S. de Melo, F. B. Dias, M. J. Calhorda, A. L. Maçanita, J. Morgado and P. T. Gomes, Luminescent halogen-substituted 2-(N-arylimino)pyrrolyl boron complexes: the internal heavy-atom effect, *Dalton Trans.*, 2020, **49**, 10185–10202; (i) P. Krishnamoorthy, C. B. Fialho, T. F. C. Cruz, A. I. Rodrigues, B. Ferreira, C. S. B. Gomes, D. Vila-Viçosa, A. Charas, J. M. S. S. Esperança, L. F. Vieira Ferreira, M. J. Calhorda, A. L. Maçanita, J. Morgado and P. T. Gomes, New luminescent tetracoordinate boron complexes: an in-depth experimental and theoretical characterisation and their application in OLEDs, *Inorg. Chem. Front.*, 2021, **8**, 3960–3983.
- 16 (a) C. S. B. Gomes, P. T. Gomes, M. T. Duarte, R. E. Di Paolo, A. L. Maçanita and M. J. Calhorda, Synthesis, Structure, and Photophysical Characterization of Blue-Green Luminescent Zinc Complexes Containing 2-Iminophenanthropyrrrolyl Ligands, *Inorg. Chem.*, 2009, **48**, 11176–11186; (b) C. S. B. Gomes, M. T. Duarte and P. T. Gomes, Further iminopyrrolyl complexes of nickel, cobalt, iron and copper: synthesis and structural characterization, *J. Organomet. Chem.*, 2014, **760**, 167–176; (c) S. A. Carabineiro, R. A. Bellabarba, P. T. Gomes, S. I. Pascu, L. F. Veiros, C. Freire, L. C. J. Pereira, R. T. Henriques, M. C. Oliveira, J. C. Warren and J. C. Synthesis, Structure and Magnetic Behavior of Five-coordinate Bis(iminopyrrolyl) Complexes of Cobalt(II) Containing PMe_3 and THF Ligands, *Inorg. Chem.*, 2008, **47**, 8896–8911.

- 17 S. A. Carabineiro, L. C. Silva, P. T. Gomes, L. C. J. Pereira, L. F. Veiros, S. I. Pascu, M. T. Duarte, S. Namorado and R. T. Henriques, Synthesis and Characterization of Tetrahedral and Square Planar Bis(iminopyrrolyl) Complexes of Cobalt(II), *Inorg. Chem.*, 2007, **46**, 6880–6890.
- 18 T. F. C. Cruz, C. A. Figueira, J. C. Waerenborgh, L. C. J. Pereira, Y. Li, R. Lescouëzec and P. T. Gomes, Synthesis, characterization and magnetism of homoleptic bis(5-aryl-2-iminopyrrolyl) complexes of iron(II) and cobalt(II), *Polyhedron*, 2018, **152**, 179–187.
- 19 (a) D. M. Bailey, R. E. Johnson and N. F. Albertson, Ethyl pyrrole 2-carboxylate, *Org. Synth.*, 1971, **51**, 100–102; (b) W. H. Harman, T. D. Harris, D. E. Freedman, H. Fong, A. Chang, J. D. Rinehart, A. Ozarowski, M. T. Sougrati, F. Grandjean, G. J. Long, J. R. Long and C. J. Chang, Slow Magnetic Relaxation in a Family of Trigonal Pyramidal Iron(II) Pyrrolide Complexes, *J. Am. Chem. Soc.*, 2010, **132**, 18115–18126; (c) E. R. King, E. T. Hennessy and T. A. Betley, Catalytic C–H Bond Amination from High-Spin Iron Imido Complexes, *J. Am. Chem. Soc.*, 2011, **133**, 4917–4923.
- 20 D. O. Garrido, G. Buldain and B. Frydman, 1,4-Diaminoalkanes from pyrroles. A new synthetic approach to substituted putrescines, *J. Org. Chem.*, 1984, **49**, 2619–2622.
- 21 (a) D. F. Evans, The determination of the paramagnetic susceptibility of substances in solution by nuclear magnetic resonance, *J. Chem. Soc.*, 1959, 2003–2005; (b) S. K. Sur, Measurement of magnetic susceptibility and magnetic moment of paramagnetic molecules in solution by high-field fourier transform NMR spectroscopy, *J. Magn. Reson.*, 1989, **82**, 169–173.
- 22 (a) S. D. Reid, A. J. Blake, C. Wilson and J. B. Love, Syntheses and Structures of Dinuclear Double-Stranded Helicates of Divalent Manganese, Iron, Cobalt, and Zinc, *Inorg. Chem.*, 2006, **45**, 636–643; (b) J. A. Wolny, M. F. Rudolf, Z. Ciunik, K. Gatner and S. Wolowicz, Cobalt(II) triazene 1-oxide bis(chelates). A case of planar (low spin)–tetrahedral (high spin) isomerism, *J. Chem. Soc., Dalton Trans.*, 1993, 1611–1622; (c) B. S. Manhas, B. C. Verma and S. B. Kalia, Spectral and magnetic studies on normal cobalt(II) planar and cobalt(III) octahedral, spin-crossover cobalt(III) octahedral and planar-tetrahedral cobalt(II) carbodithioates, *Polyhedron*, 1995, **14**, 3549–3556; (d) B. S. Jaynes, L. H. Doerrer, S. Liu and S. J. Lippard, Synthesis, Tuning of the Stereochemistry, and Physical Properties of Cobalt(II) Tropocoronand Complexes, *Inorg. Chem.*, 1995, **34**, 5735–5744; (e) F. A. Cotton and G. Wilkinson, *Advanced Inorganic Chemistry*, John Wiley and Sons, New York, 6th edn, 1999, p. 821; (f) N. N. Greenwood and A. Earnshaw, *Chemistry of the Elements*, Elsevier Butterworth-Heinemann, 2nd edn, 1997, p. 1113.
- 23 L. Yang, D. R. Powell and R. P. Houser, Structural variation in copper(I) complexes with pyridylmethylamide ligands: structural analysis with a new four-coordinate geometry index, τ_4 , *Dalton Trans.*, 2007, 955–964.
- 24 A. Sarkar, S. Tewary, S. Sinkar and G. Rajaraman, Magnetic Anisotropy in $\text{Co}^{\text{II}}\text{X}_4$ (X = O, S, Se) Single-Ion Magnets: Role of Structural Distortions versus Heavy Atom Effect, *Chem. – Asian J.*, 2019, **14**, 4696–4704.
- 25 M. Murrie, Cobalt(II) single-molecule magnets, *Chem. Soc. Rev.*, 2010, **39**, 1986–1995.
- 26 L. Pardi, J. Krzystek, J. Telser and L. Brunel, Multifrequency EPR Spectra of Molecular Oxygen in Solid Air, *J. Magn. Reson.*, 2000, **146**, 375–378.
- 27 M. Atanasov, D. Ganyushin, K. Sivalingam and F. Neese, A modern first-principles view on ligand field theory through the eyes of correlated multireference wavefunctions, in *Molecular Electronic Structures of Transition Metal Complexes II*, ed. D. M. P. Mingos, P. Day and J. P. Dahl, Springer Berlin Heidelberg, Berlin, Heidelberg, 2012, pp. 149–220.
- 28 R. Boča, Zero-field splitting in metal complexes, *Coord. Chem. Rev.*, 2004, **248**, 757–815.
- 29 A. Sarkar, S. Dey and G. Rajaraman, Role of Coordination Number and Geometry in Controlling the Magnetic Anisotropy in Fe^{II} , Co^{II} , and Ni^{II} Single-Ion Magnets, *Chem. – Eur. J.*, 2020, **26**, 14036–14058.
- 30 (a) W. Huang, T. Liu, D. Wu, J. Cheng, Z. W. Ouyang and C. Duan, Field-induced slow relaxation of magnetization in a tetrahedral Co(II) complex with easy plane anisotropy, *Dalton Trans.*, 2013, **42**, 15326–15331; (b) F. Yang, Q. Zhou, Y. Zhang, G. Zeng, G. Li, Z. Shi, B. Wang and S. Feng, Inspiration from old molecules: field-induced slow magnetic relaxation in three air-stable tetrahedral cobalt(II) compounds, *Chem. Commun.*, 2013, **49**, 5289–5291; (c) M. R. Saber and K. R. Dunbar, Ligands effects on the magnetic anisotropy of tetrahedral cobalt complexes, *Chem. Commun.*, 2014, **50**, 12266–12269; (d) A. K. Mondal, M. Sundararajan and S. Konar, A new series of tetrahedral Co(II) complexes $[\text{CoLX}_2]$ (X = NCS, Cl, Br, I) manifesting single-ion magnet features, *Dalton Trans.*, 2018, **47**, 3745–3754; (e) Y. Zhai, Y. Deng and Y. Zheng, Pseudotetrahedral cobalt(II) complexes with PNP-ligands showing uniaxial magnetic anisotropy, *Dalton Trans.*, 2018, **47**, 8874–8878.
- 31 (a) C. Benelli and D. Gatteschi, *Introduction to Molecular Magnetism: from transition metals to lanthanides*, Wiley-VCH, 1st edn, 2015; (b) C. Boskovic, E. K. Brechin, W. E. Streib, K. Folting, J. C. Bollinger, D. N. Hendrickson and G. Christou, Single-Molecule Magnets: A New Family of Mn_{12} Clusters of Formula $[\text{Mn}_{12}\text{O}_8\text{X}_4(\text{O}_2\text{CPh})_8\text{L}_6]$, *J. Am. Chem. Soc.*, 2002, **124**, 3725–3736.
- 32 A. Abragam and B. Bleaney, *Electron Paramagnetic Resonance of Transition Ions*, Dover Publications, 1986.
- 33 For example: (a) P. T. Gomes, M. L. H. Green and A. M. Martins, Ansa-bridged η -cyclopentadienyl imido and amido derivatives of titanium, zirconium and molybdenum, *J. Organomet. Chem.*, 1998, **551**, 133–138; (b) M. M. Marques, S. Fernandes, S. G. Correia, J. R. Ascenso, S. Caroço, P. T. Gomes, J. F. Mano, S. G. Pereira, T. Nunes, A. R. Dias, M. D. Rausch and

- J. C. W. Chien, Synthesis of acrylamide/olefin copolymers by a diimine nickel catalyst, *Macromol. Chem. Phys.*, 2000, **201**, 2464–2468; (c) R. Garçon, C. Clerck, J.-P. Gesson, J. Bordado, T. Nunes, S. Carçoço, P. T. Gomes, M. E. M. da Piedade and A. P. Rauter, Synthesis of novel polyurethanes from sugars and 1,6-hexamethylene diisocyanate, *Carbohydr. Polym.*, 2001, **45**, 123–127; (d) V. Rosa, P. J. Gonzalez, T. Avilés, P. T. Gomes, R. Welter, A. C. Rizzi, M. C. G. Passeggi and C. D. Brondino, Synthesis, solid-state structures, and EPR spectroscopic studies on polycrystalline and single-crystal samples of alpha-diimine cobalt(II) complexes, *Eur. J. Inorg. Chem.*, 2006, 4761–4769.
- 34 SAINT Software for the CCD Detector System, Version 7.03, Bruker AXS Inc., Madison, WI, USA, 2004.
- 35 G. M. Sheldrick, *SADABS, Program for Empirical Absorption Correction*, University of Göttingen, Göttingen, Germany, 1996.
- 36 M. C. Burla, R. Caliandro, B. Carrozzini, G. L. Cascarano, C. Cuocci, C. Giacovazzo, M. Mallamo, A. Mazzone and G. Polidori, Crystal structure determination and refinement via SIR2014, *J. Appl. Crystallogr.*, 2015, **48**, 306–309.
- 37 (a) G. M. Sheldrick, Crystal structure refinement with SHELXL, *Acta Crystallogr., Sect. C: Struct. Chem.*, 2015, **71**, 3–8; (b) C. B. Hübschle, G. M. Sheldrick and B. Dittrich, ShelXle: a Qt graphical user interface for SHELXL, *J. Appl. Crystallogr.*, 2011, **44**, 1281–1284.
- 38 (a) L. J. Farrugia, WinGX suite for small-molecule single-crystal crystallography, *J. Appl. Crystallogr.*, 1999, **32**, 837–838; (b) L. J. Farrugia, WinGX and ORTEP for Windows: an update, *J. Appl. Crystallogr.*, 2012, **45**, 849–854.
- 39 (a) M. N. Burnett and C. K. Johnson, *ORTEP-III: Oak Ridge Thermal Ellipsoid Plot Program for Crystal Structure Illustration*, Oak Ridge National Laboratory, 1996, p. 6895; (b) L. J. Farrugia, ORTEP-3 for Windows—A Version of It ORTEP-III with a Graphical User Interface (GUI), *J. Appl. Crystallogr.*, 1997, **30**, 565.
- 40 P. Neugebauer, D. Bloos, R. Marx, P. Lutz, M. Kern, D. Aguilà, J. Vaverka, O. Laguta, C. Dietrich, R. Clérac and J. van Slageren, Ultra-broadband EPR spectroscopy in field and frequency domains, *Phys. Chem. Chem. Phys.*, 2018, **20**, 15528–15534.
- 41 F. Neese, Software update: the ORCA program system, version 4.0, *Wiley Interdiscip. Rev.: Comput. Mol. Sci.*, 2017, **8**, e1327.
- 42 C. Angeli, R. Cimiraglia, S. Evangelisti, T. Leininger and J.-P. Malrieu, Introduction of n-electron valence states for multireference perturbation theory, *J. Chem. Phys.*, 2001, **114**, 10252–10264.
- 43 C. Angeli, R. Cimiraglia and J.-P. Malrieu, N-electron valence state perturbation theory: a fast implementation of the strongly contracted variant, *Chem. Phys. Lett.*, 2001, **350**, 297–305.
- 44 O. Vahtras, J. Almlöf and M. W. Feyereisen, Integral approximations for LCAO-SCF calculations, *Chem. Phys. Lett.*, 1993, **213**, 514–518.
- 45 B. O. Roos, The Complete Active Space Self-Consistent Field Method and its Applications in Electronic Structure Calculations, in *Adv. Chem. Phys.*, ed. K. P. Lawley, John Wiley & Sons, Inc., 1987, pp. 399–445.
- 46 C. Angeli, S. Borini, M. Cestari and R. Cimiraglia, A quasi-degenerate formulation of the second order n-electron valence state perturbation theory approach, *J. Chem. Phys.*, 2004, **121**, 4043–4049.
- 47 H. Nakano, Quasidegenerate perturbation theory with multiconfigurational self-consistent-field reference functions, *J. Chem. Phys.*, 1993, **99**, 7983–7992.
- 48 S. Kossmann and F. Neese, Comparison of two efficient approximate Hartree–Fock approaches, *Chem. Phys. Lett.*, 2009, **481**, 240–243.
- 49 F. Neese, F. Wennmohs, A. Hansen and U. Becker, Efficient, approximate and parallel Hartree–Fock and hybrid DFT calculations. A ‘chain-of-spheres’ algorithm for the Hartree–Fock exchange, *Chem. Phys.*, 2009, **356**, 98–109.
- 50 B. A. Hess, Relativistic electronic-structure calculations employing a two-component no-pair formalism with external-field projection operators, *Phys. Rev. A*, 1986, **33**, 3742–3748.
- 51 G. Jansen and B. A. Hess, Revision of the Douglas-Kroll transformation, *Phys. Rev. A*, 1989, **39**, 6016–6017.
- 52 N. Douglas and N. M. Kroll, Quantum electrodynamic corrections to fine-structure of helium, *Ann. Phys.*, 1974, **82**, 89–155.
- 53 A. Hellweg, C. Hättig, S. Höfener and W. Klopper, Optimized accurate auxiliary basis sets for RI-MP2 and RI-CC2 calculations for the atoms Rb to Rn, *Theor. Chem. Acc.*, 2007, **117**, 587–597.
- 54 F. Weigend, Accurate Coulomb-fitting basis sets for H to Rn, *Phys. Chem. Chem. Phys.*, 2006, **8**, 1057–1065.
- 55 B. A. Heß, C. M. Marian, U. Wahlgren and O. Gropen, A mean-field spin-orbit method applicable to correlated wavefunctions, *Chem. Phys. Lett.*, 1996, **251**, 365–371.
- 56 F. Neese, Efficient and accurate approximations to the molecular spin-orbit coupling operator and their use in molecular g-tensor calculations, *J. Chem. Phys.*, 2005, **122**, 034107.
- 57 V. Vallet, L. Maron, C. Teichteil and J. P. Flament, A two-step uncontracted determinantal effective Hamiltonian-based SO–CI method, *J. Chem. Phys.*, 2000, **113**, 1391–1402.
- 58 R. L. Carlin, *Magnetochemistry*, Springer, Berlin, 1986.